ELSEVIER

Contents lists available at ScienceDirect

### Materials & Design

journal homepage: www.elsevier.com/locate/matdes



# *In vitro* degradation behavior of novel Zn–Cu–Li alloys: Roles of alloy composition and rolling processing



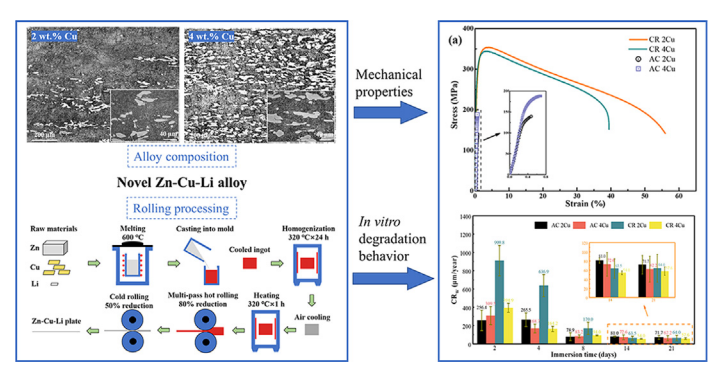
Shiyu Huang a, Luning Wang b, Yufeng Zheng c, Lijie Qiao a,\*, Yu Yan a,\*

- <sup>a</sup> Beijing Advanced Innovation Center for Materials Genome Engineering, Corrosion and Protection Center, Institute for Advanced Materials and Technology, University of Science and Technology Beijing, 100083, China
- <sup>b</sup> Beijing Advanced Innovation Center for Materials Genome Engineering, School of Materials Science and Engineering, University of Science and Technology Beijing, Beijing 100083, China
- <sup>c</sup> Department of Materials Science and Engineering, College of Engineering, Peking University, Beijing 100871, China

#### HIGHLIGHTS

- Four key effects of Cu addition on corrosion behavior of Zn-alloy are revealed.
- Cu addition and rolling jointly alter the corrosion mode from localized to
- Cold-rolled Zn-4Cu-0.02Li possesses proper mechanical and degradation properties.

## G R A P H I C A L A B S T R A C T



#### ARTICLE INFO

Article history:
Received 9 September 2021
Revised 21 October 2021
Accepted 26 November 2021
Available online 27 November 2021

Keywords: Biodegradable metal Zn-Cu alloy Corrosion products Simulated body fluid Rolling

#### ABSTRACT

Zn-alloys are considered to be promising biodegradable materials due to suitable degradation rates. In this paper, novel Zn-Cu-Li alloys with layered  $CuZn_4$  structure were achieved. The corrosion properties of newly developed biodegradable Zn-Cu-Li alloys in simulated body fluid was studied. Results indicated that the cold-rolled alloys presented a relatively uniform corrosion mode, although early corrosion occurred preferentially at phase boundaries. Galvanic corrosion and corrosion product films jointly determined the later corrosion process. Cu improved the corrosion potential and film properties in its solid solution state, induced galvanic corrosion, and provided a physical barrier to corrosion by forming  $CuZn_4$  phase. Rolling accelerated the initial corrosion rate by enhancing the matrix electrochemical activity, while it contributed to uniform corrosion by improving the  $CuZn_4$  phase shape. Finally, cold-rolled  $Zn_4$  contributed to uniform corrosion resistance and mechanical properties combination among the prepared alloys, with a yield strength of 256 MPa, an ultimate strength of 342 MPa, a fracture elongation of 39.8 %, and a corrosion rate of nearly 55  $\mu$ m/year.

© 2021 Published by Elsevier Ltd. This is an open access article under the CC BY-NC-ND license (http://creativecommons.org/licenses/by-nc-nd/4.0/).

#### 1. Introduction

Zinc (Zn) as a biodegradable metal material has gradually attracted the attention of the medical industry and research institutions due to its exceptional biocompatibility and physiological degradation [1–3]. Insufficient mechanical properties of pure Zn, however, lead to an urgent need for the development and

E-mail addresses: lqiao@ustb.edu.cn (L. Qiao), yanyu@ustb.edu.cn (Y. Yan).

<sup>\*</sup> Corresponding authors.

application of new Zn based alloys [4]. Among them, Zn-Cu alloys, with high plasticity, outstanding antibacterial properties, and reasonable degradation rates have become one of the research hotspots in the field of degradable metals in recent years [5-7]. Furthermore, trace addition of a third element (such as 0.02 wt% Li) can enhance the strength and reduce the loss of plasticity of the Zn-Cu alloy, which can improve its mechanical properties [8]. Nevertheless, corrosion is an inevitable problem during application. It is worth noting that many scholars use "corrosion" to describe the in vitro degradation behavior of biomedical metals when the corrosion test methods of industrial metals are used to evaluate the degradation performance [9-10]. Surface modification has been considered as a good method to control the corrosion and biocompatibility of biomedical metals [11–13]. However, understanding corrosion mechanisms and key influencing factors of the Zn-Cu alloys is beneficial in the optimization of their corrosion resistance.

The effects of Cu on the corrosion rate or mode of the alloy are controversial. It has been reported that the addition of Cu has little effect on the corrosion rate [14], but a previous study has confirmed that the presence of Cu can cause galvanic corrosion and accelerate corrosion [15]. Lin et al. [16-17] summarized the dual roles of the CuZn<sub>5</sub> second phase: one is to cause galvanic corrosion, and the other is to exert a barrier effect against corrosion through network distribution. In addition, uniform and localized corrosion behavior of Zn-Cu alloys were also described. Zn-Cu alloys, with refined grains and a uniformly distributed second phase, trended to homogeneous corrosion [18]. In contrast, Chen et al. [19] proposed that the corrosion process occurred preferentially in the second phase precipitation area. Zhou et al. [20] also reported localized degradation of a Zn-0.8Cu stent implantation in pig coronary artery after 9 months. In view of the debate, the corrosion behavior of Zn-Cu alloys in the physiological environment needs to be fully understood for the safety and versatility of implants.

Deformation processes are usually necessary in the preparation of Zn-Cu alloys, but their influence on corrosion of the alloy is difficult to predict. Different studies have deemed that extrusion and hot rolling process can increase [21–22] or decrease [23–24] the corrosion rate of Zn. In addition, rolling has been supposed to be responsible for the improvement of localized corrosion [18]. In general, processing history affects the corrosion behavior of Zn alloys mainly by changing the microstructure. The corrosion rate of a deformed alloy with fine grains is lower than that of a coarse-grained alloy [23,25]. The impacts of deformation on the corrosion behavior of Zn-Cu alloys have rarely been discussed in detail. However, implants are inevitably subjected to varying degrees of deformation in the process of production, implantation, and service. Thus, understanding the effect of deformation processes on corrosion behavior of Zn-Cu alloy is of great importance.

In this study, the effects of alloy composition and deformation processes on the microstructure, mechanical properties, and corrosion behavior of Zn–Cu–Li alloys were examined. The microstructure of the alloys was studied in detail by a scanning electron microscope (SEM), an energy disperse spectroscope (EDS), X-ray diffraction (XRD) apparatus, and a transmission electron microscope (TEM). The corrosion resistance was evaluated systematically by electrochemistry, scanning Kelvin probe force microscope (SKPFM), and immersion tests. Corrosion products were analyzed by SEM, EDS, XRD, and X-ray photoelectron spectroscope (XPS).

#### 2. Materials and methods

#### 2.1. Material preparation

Zn-2 wt.%Cu-0.02 wt.%Li and Zn-4 wt.%Cu-0.02 wt.%Li alloys, abbreviated as 2Cu and 4Cu respectively, were prepared with high

purity Zn (99.95 wt%), Cu (99.95 wt%), and Li (99.95 wt%) metals. The alloy preparation process is briefly shown in Fig. 1. The raw materials were melted in a ZG–0.01 vacuum induction furnace under the protection of argon. The melt was kept at 650 °C for 40 min, poured into a graphite mold, and cooled in air to obtain a cylinder ingot. All ingots were homogenized at 320 °C for 24 h and then cooled in air. Then the homogenized alloys were hot rolled at 320 °C from 20 mm down to 4 mm thickness by 7 passes with intermediate annealing, achieving an 80% reduction. Finally, the hot-rolled plates were cold rolled into 2-mm thick sheets using one pass, to achieve a total reduction of 90%. The actual composition of the alloys listed in Table 1 was determined by inductively coupled plasma atomic emission spectrometry. It should be noted that Fe with a content of less than 0.1 wt% is considered as an impurity element, as in an agreement with other reports [17,26].

#### 2.2. Microstructure characterization

For characterization,  $10 \times 10 \times 2$  mm specimens of the as-cast (AC) and cold-rolled (CR) Zn–Cu–Li were cut and mechanically ground to 5000 grits, then polished to obtain a mirror-like surface with 0.5 µm diamond paste. The polished samples were finally electropolished in an acidic solution (1 g oxalic acid, 1 mL acetic acid, 1 mL nitric acid, and 150 mL deionized water) at a constant current of 0.5 A for 2–10 s. The microstructure of the ground and polished alloys was characterized by metallurgical microscope (Olympus, BX60M) and Zeiss Merlin FE-SEM coupled with an EDS analyzer. The phase identification of the alloys was analyzed by XRD with Jade 5.0 software. XRD analysis was carried out on an TZY-Xrd (D/MAX-TTRIII) with Cu K $\alpha$  radiation (0.1542 nm), in step scanning mode ( $10^{\circ}$ /min) from  $10^{\circ}$  to  $90^{\circ}$ .

TEM technique was used to further characterize the second phase of the alloys. Plates with a thickness of 0.5 mm were cut and ground up to 2000 grits until the thickness was reduced to 50  $\mu$ m. Disks of 3 mm in diameter were punched from thin foils of 50  $\mu$ m and thinned by ion beam. TEM observations were conducted on a FEI Tecnai G2 F20 microscope operated at 200 kV, and the acquired selected area electron diffraction (SAED) patterns were analyzed using a Digital Micrograph.

#### 2.3. Mechanical test and fracture analysis

Samples for tensile tests were prepared according to ISO 6892–1: 2009. The specimens were machined along the casting or rolling direction with a gauge size of 10 mm (length)  $\times$  3 mm (width)  $\times$  2 mm (thickness). Prior to each test, specimens were ground with SiC papers up to 5000 grits and ultrasonically cleaned in acetone and ethanol. Then, the tensile tests were performed on an CMT 6000 machine at constant strain rate of  $1 \times 10^{-3}$  s<sup>-1</sup>. The tensile yield strength (*YS*) was the stress at 0.2% plastic deformation, the ultimate tensile strength (*UTS*) and the elongation at fracture (*E*) were obtained from the stress–strain curves. In addition, the fracture surfaces were observed by Zeiss Merlin FE-SEM coupled with an EDS analyzer. The center region with higher stress, the edge region with lower stress, and the characteristic fracture region of the second phase were accordingly determined.

#### 2.4. Electrochemical measurement

Electrochemical measurements were conducted on an electrochemical analyzer (ModuLab XM). Tests were performed in the SBF (142.0 mmol/L Na<sup>+</sup>, 5.0 mmol/L K<sup>+</sup>, 2.5 mmol/L Ca<sup>2+</sup>, 1.5 mmol/L Mg<sup>2+</sup>, 147.8 mmol/L Cl<sup>-</sup>, 4.2 mmol/L HCO<sub>3</sub>, 1.0 mmol/L HPO<sub>4</sub><sup>2-</sup>, and 0.5 mmol/L SO<sub>4</sub><sup>2-</sup>) with a Tris-HCl buffer system at 37 °C. The pH value of the SBF was adjusted to 7.4 with the addition of 1 M NaOH or HCl. A three-electrode cell containing

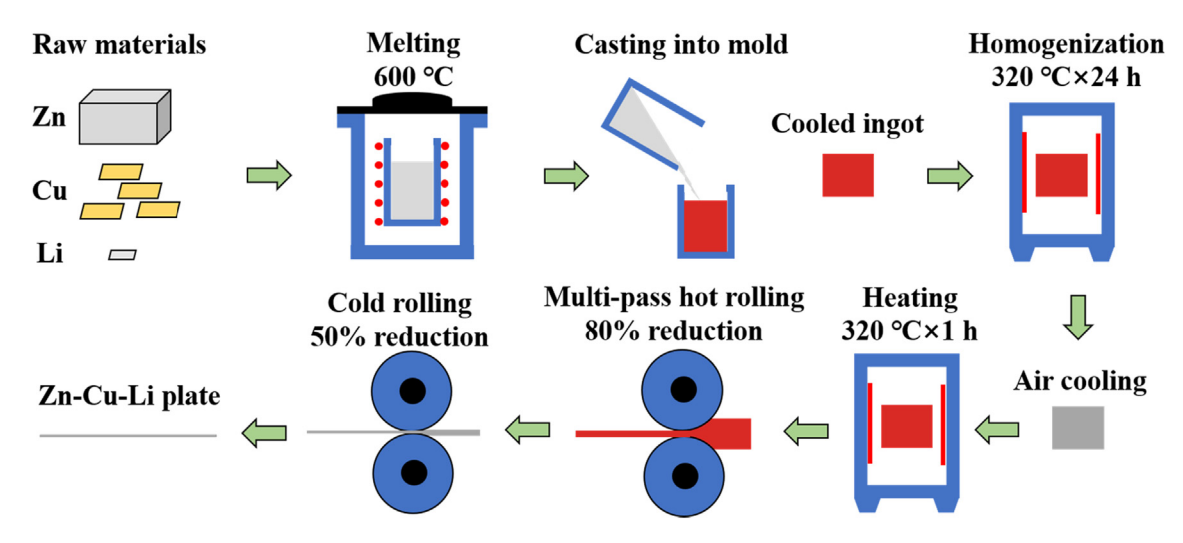


Fig. 1. Schematic diagram of the alloy preparation route.

**Table 1**The nominal and measured chemical compositions of alloys.

Alloys	Cu (wt.%)	Li (wt.%)	Fe (wt.%)	Ni (wt.%)	Zn (wt.%)
Zn-2Cu-0.02Li (2Cu)	1.94	0.026	0.041	<0.005	97.90
Zn-4Cu-0.02Li (4Cu)	3.90	0.017	0.079	0.0079	95.99

250~mL of electrolyte, using the alloy samples as the working electrode, Pt plate as the counter electrode, and a saturated calomel electrode (SCE) as the reference electrode was employed. The working electrode with the dimension of  $\phi 10 \times 2~mm$  was electrically connected with copper wire and then sealed with epoxy resin to expose the research surface area (ca.  $3.14~cm^2$ ). All the samples were mechanically ground to 5000~grits, polished to obtain a mirror-like surface by using  $0.5~\mu m$  diamond paste, rinsed in ethanol and ultrapure water to remove the surface contaminants, and dried.

In all tests, the working electrode was equilibrated at open circuit potential (OCP) for 20 min. Electrochemical impedance spectroscopy (EIS) spectra were measured at the OCP of  $\pm$  10 mV sinusoidal amplitude in the frequency range of 100 kHz to 100 mHz. The EIS data were analyzed using ZsimDemo software. Potentiodynamic polarization (PDP) tests were conducted in a potential range of -0.2 V  $_{\rm vs.\ OCP}$  to -0.8 V  $_{\rm vs.\ SCE}$  at a constant scan rate of 1 mV/s. Each test was repeated for three times to ensure accuracy. The corrosion current density  $i_{corr}$  was determined by the Tafel method through linear extrapolation, which could be further converted to the corrosion rate ( $CR_F$ , mm/year) as below:

$$CR_E = \frac{315.36 \times ai_{corr}}{nFD} \tag{1}$$

where a (g/mol) is the atomic weight, n is number of equivalent exchange, F (C/mol) is the Faraday's constant, D (g/cm³) is the density of the material. The densities of the alloys were determined by the Archimedes drainage method.

#### 2.5. SKPFM measurement

The relationship between microstructure heterogeneity (such as second phase and triple junctions) and corrosion resistance was revealed by SKPFM. In general, higher electron work function reflected by higher Volta potential obtained by SKPFM refers to higher corrosion resistance [27–28]. Block samples with a dimension of  $10 \times 10 \times 2$  mm were cut from the raw materials, ground,

mechanically polished, and electropolished. The surface Volta potential was obtained using SKPFM with a Dimension Nanoscope V from Veeco Instruments Inc., using lift mode to record a secondary channel and a scan rate of 0.5 Hz. All measurements were conducted in air at room temperature with a humidity close to 20% RH.

#### 2.6. Immersion test

Immersion tests were carried out in SBF according to ASTM G31–72 using a ratio of solution volume to sample area of 20 mL/cm $^2$ . The 10  $\times$  10  $\times$  2 mm specimens were placed in 100 mL centrifuge tubes and soaked in 70 mL SBF at 37 °C. The SBF solution was replaced every two days to constrain ion consumption and rapid pH change. Testing was performed at 2, 4, 8, 14 and 21 days. Four plates were removed from the centrifuge tubes at each point: three were used to calculate the corrosion rate and one was used to analyze corrosion products and surface profile.

The corroded samples were cleaned in 100 g/L NH<sub>4</sub>Cl for 2–5 min at 70 °C according to ISO 8407: 2009, washed with ethyl alcohol, and dried to acquire the final weight. According to ASTM–G31–12a, the corrosion rate ( $CR_W$ , mm/year) was calculated by the weight loss method using the following formula [29],

$$CR_W = \frac{87.6 \times (W_0 - W_t)}{DAt},$$
(2)

where  $W_0$  (mg) and  $W_t$  (mg) are the initial weight before immersion and the final weight after immersion respectively, D (g/cm<sup>3</sup>) is the density of the alloys, A (cm<sup>2</sup>) is the total sample surface area, and t (h) is the immersion time.

Surface and cross-section morphologies of the samples were examined by Zeiss Merlin FE-SEM coupled with an EDS analyzer. The phase of the corrosion products was identified by XRD and XPS, using the same XRD measurement process described above. XPS tests were conducted on a Thermo Scientific Escalab 250Xi. All peaks were corrected with the standard C 1s binding energy

(284.8 eV), and the XPS data were analyzed by XPS PEAK 4.1 software. Finally, corrosion morphologies were observed by SEM after the removal of corrosion product film (CPF).

#### 2.7. Fluorescence staining and cell morphology

Human umbilical vein endothelial cells (HUVECs) were adopted to preliminarily evaluate the cytocompatibility of CR 2Cu and 4Cu alloys. HUVECs were cultured in Dulbecco's modified Eagle's medium (DMEM) containing 10% fetal bovine serum (FBS) and 1% penicillin–streptomycin (PS) in humidified atmosphere of 5% CO $_2$  at 37  $^{\circ}\mathrm{C}$  for 48 h. Materials extracts were collected by immersing the samples in DMEM cell culture medium with a surface area to medium ratio of 1.25 cm²/mL under standard cell culture condition for 48 h. Afterward, the collected extract solutions were diluted into 50% and 10% extract with cell culture media.

To investigate the cell morphology, 1 mL cell suspension was seeded in 24-well plates at a density of 5  $\times$  10<sup>4</sup> cell/mL and cultured for 24 h to allow attachment. Then the medium in each well was replaced with 1 mL 100%, 50% and 10% sample extracts and cells were incubated for another 5 days. Culture media without extract media was used as the control. Subsequently, the medium was removed and cells were washed 2 times with PBS. Cell membranes were stained with 3,3'-dioctadecyloxacarbocyanine perchlorate (DIO, Beyotime, Shanghai, China) for 10 min at 37°C and washed with PBS. Then the cells were fixed with 4% paraformaldehyde (Beyotime, Shanghai, China) at room temperature for 15 min and washed with PBS. Nucleus was counterstained with 10  $\mu g/mL$  4',6-diamidino-2-phenylindole (DAPI, Beyotime, Shanghai, China) for 10 min in the dark. After rinsing with PBS, the samples were observed under confocal microscopy.

#### 3. Results

#### 3.1. Microstructure analysis

Fig. 2a1 and 2b1 show the microstructures of the AC 2Cu and 4Cu alloys, respectively. The matrix was Zn–Cu solid solution, in which the atomic percentage of Cu was about 4 at.%. Dendritic particles (butterfly and oval shapes) can be seen within grains or grain boundaries. The EDS results prove that the Cu-enriched (14.37 at. %) particles are CuZn<sub>4</sub>, whose Zn/Cu atomic ratio ranges from 4 to 7 [30]. The results also show that the volume fraction of CuZn<sub>4</sub> increased with an increase of Cu content. According to the Zn–Cu binary phase diagram [31], primary Zn is formed first, and then CuZn<sub>4</sub> is formed after precipitation transformation in 2Cu alloy. However, the primary Zn phase of 4Cu alloy is formed by peritectic reaction between liquid phase and CuZn<sub>4</sub> phase.

In addition, the needle-like precipitates marked with blue arrows in Fig. 2a1 and 2b1 are considered to be LiZn<sub>4</sub>. Although Li as a light element is unable to be detected by EDS, the Zn–Li phase diagram [32] shows the existence of  $\beta$  LiZn<sub>4</sub> phase in Zn–X wt.%Cu–0.02 wt.%Li alloys (X = 2 or 4). When Li content is 0.02 wt%, there is no eutectic reaction during equilibrium solidification process. The LiZn<sub>4</sub> precipitates are distributed around the primary Zn phase due to exsolution effect. XRD patterns in Fig. 2c show that all of the Zn–Cu–Li alloys were composed of Zn, CuZn<sub>4</sub>, and LiZn<sub>4</sub> phases. Notably, the diffraction peaks of the LiZn<sub>4</sub> phase are weak due to its low content.

As for the microstructure of CR 2Cu and 4Cu (Fig. 2a2 and 2b2), the  $CuZn_4$  particles were stretched along the rolling direction, part of which was broken.  $LiZn_4$ , however, was difficult to be observed after cold deformation. The shape of the second phases was changed significantly after wrought processing. Uniquely, the cross section of the CR alloys (Fig. 2a3 and 2b3) presents a laminated

structure, separated by an elongated CuZn<sub>4</sub> second phase. This layered structure is expected to have a profound impact on the corrosion behavior. TEM investigation was carried out to further explore the microstructure of the second phase. Sizes of butterfly shaped and oval shaped cross sections of CuZn<sub>4</sub> particles varied over a wide range, as shown in Fig. 2d1 and 2d2, with corresponding SAED shown in the figures.

#### 3.2. Mechanical properties

The mechanical properties of these alloys are shown in Fig. 3. Both CR 2Cu and CR 4Cu meet the benchmark mechanical properties of biodegradable metal materials [33]. In particular, the CR 2Cu exhibited the best mechanical properties with an extraordinarily high ductility. Deformation processes remarkably improve the strength and plasticity. The ultimate tensile strength (*UTS*) of CR 2Cu is twice that of AC 2Cu. Elongation at fracture (*E*) of the CR 2Cu reaches 49.1%, exhibiting a same brittle-to-ductile transition as the Zn–Mn alloys reported by Shi et al [34]. Differences in Cu content also contributed to the slight dissimilarity of the mechanical properties. The *UTS* and *E* of the AC 4Cu increased by 34% and 40%, respectively, as compared to those of the AC 2Cu. After rolling, distinctions of the mechanical properties between 2Cu and 4Cu were significantly reduced.

The fracture surfaces of AC and CR specimens are shown in Fig. 4. Many cleavage planes, steps, tear ridges, river-like patterns and secondary cracks appear on the surfaces of AC alloys, see Fig. 4a1, 4a2, 4b1 and 4b2, indicating typical cleavage characteristics. Clearly, the AC alloys present a brittle fracture mode. In Fig. 4a3 and 4b3, torn CuZn<sub>4</sub> particles and needle-like LiZn<sub>4</sub> precipitates (marked by yellow and blue lines, respectively) are found to be convex in the plane, with poor bonding with the matrix. The CR samples show dimples with different sizes and almost no cleavage facets (Fig. 4c1-c2 and 4d1-d2), illustrating a micro-void accumulation fracture process. In addition, a small amount of CuZn<sub>4</sub> particle, with a Cu atomic content of 13.1 and 12.3 at.%, is detected within the dimples (Fig. 4c3 and 4d3).

#### 3.3. Electrochemical properties

Fig. 5a shows the PDP curves of the Zn-Cu-Li alloys in the SBF, with the value of the corrosion current density  $(i_{corr})$  listed in the table. For all bare alloys, the shape of PDP curves is unchanged. The extra 2 wt% Cu shifts the cathodic polarization curve to the right, as shown by comparing the curves of AC 2Cu and 4Cu. After rolling, the corrosion potential of 2Cu rises and the cathodic polarization curve shifts rightward significantly, leading to a remarkable increase in  $i_{corr}$  from 2.30  $\mu$ A/cm<sup>2</sup> to 6.01  $\mu$ A/cm<sup>2</sup>. Contrary to 2Cu, a slight right shift occurs in the anodic polarization part of CR 4Cu compared with AC 4Cu. In general, the CR alloys have a higher  $i_{corr}$ , which may be related to higher electrochemical activity resulting from the numerous lattice defects after deformation. Corrosion rate calculated from  $i_{corr}$  is present in Fig. 5b. It can be seen that the electrochemical corrosion rate of AC 4Cu is higher than that of AC 2Cu, while CR 4Cu has a notable lower corrosion rate than CR 2Cu.

The EIS results of the tested alloys in SBF are shown in Fig. 5c and 5d. From the Bode diagram, the impedance module value of all Zn–Cu–Li alloys is approximately the same. The phase angle distribution indicates that there are two peaks for samples; however, the peak frequency of AC alloys is different from that of CR alloys. This phenomenon is also reflected by the Nyquist plots shown in Fig. 5d. The spectra present two relatively regular capacitive reactance arcs with different radii, indicating different corrosion resistances. For AC alloys, two semicircle arcs are located at the high-frequency zone and mid-frequency zone, which are affected by

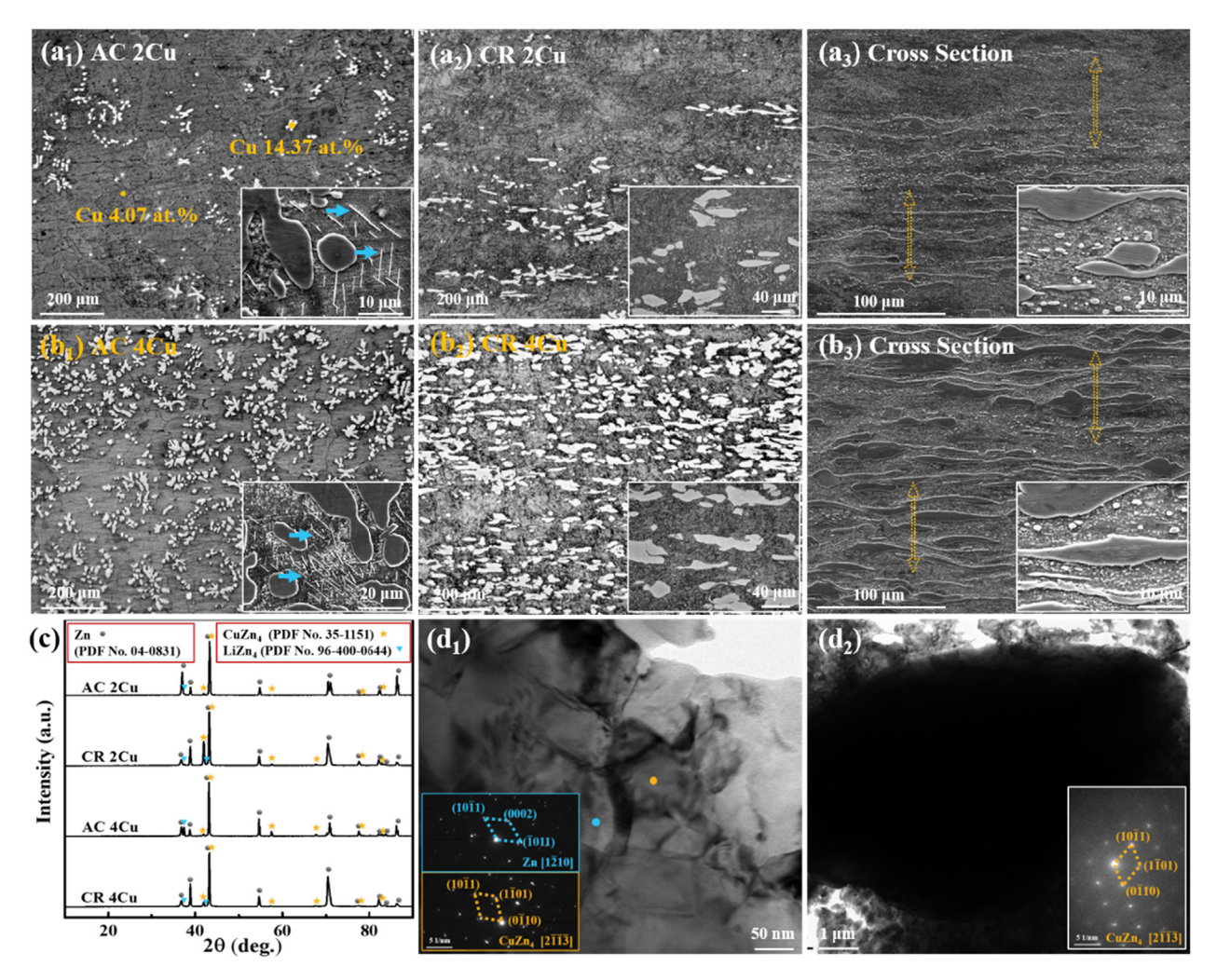


Fig. 2. Typical micrographs of (a) 2Cu and (b) 4Cu after electropolishing. Numbers 1 and 2 represent AC and CR states respectively, and 3 is the cross section of the CR alloy. (c) XRD patterns of the alloys. (d) TEM bright field images with SAED patterns of CuZn<sub>4</sub> second phase.

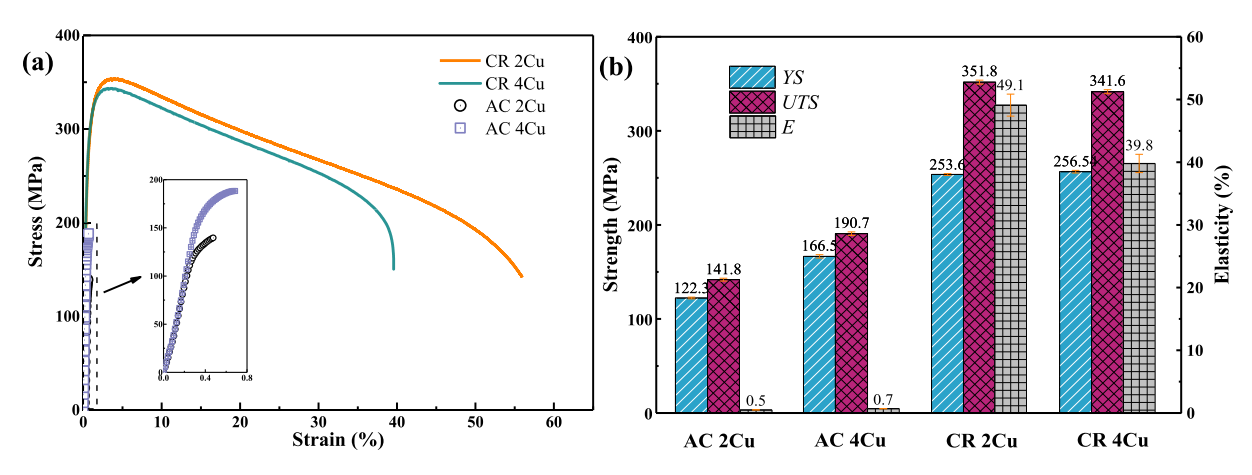


Fig. 3. Engineering stress-strain tensile curves (a) and the elongation and strength (b) of samples.

the charge transfer process and the formation of a uniform oxidation film on the surface of the specimen [14,35]. The equivalent circuit of model 1 in Fig. 5d is used to get a good fit. In this case, the electrolyte solution penetrates the surface oxide film uniformly. As for CR alloys, the low-frequency capacitive arc results from an oxidation film with micropores, while the high-frequency arc corresponds to the charge transfer process. Such characteristics can be

fitted by model 2, which is widely used for describing the impedance spectra with two time constants [35–36].

The fitting results are shown in the Table 2, in which the parameters are defined as follows:  $R_s$  is solution resistance;  $R_f$  and  $R_{ct}$  denote CPF resistance and charge transfer resistance, respectively; and  $CPE_f$  and  $CPE_{dl}$  indicate constant phase element (CPE) for the nonideal capacitance induced by CPF and by the double electrode

Materials & Design 212 (2021) 110288

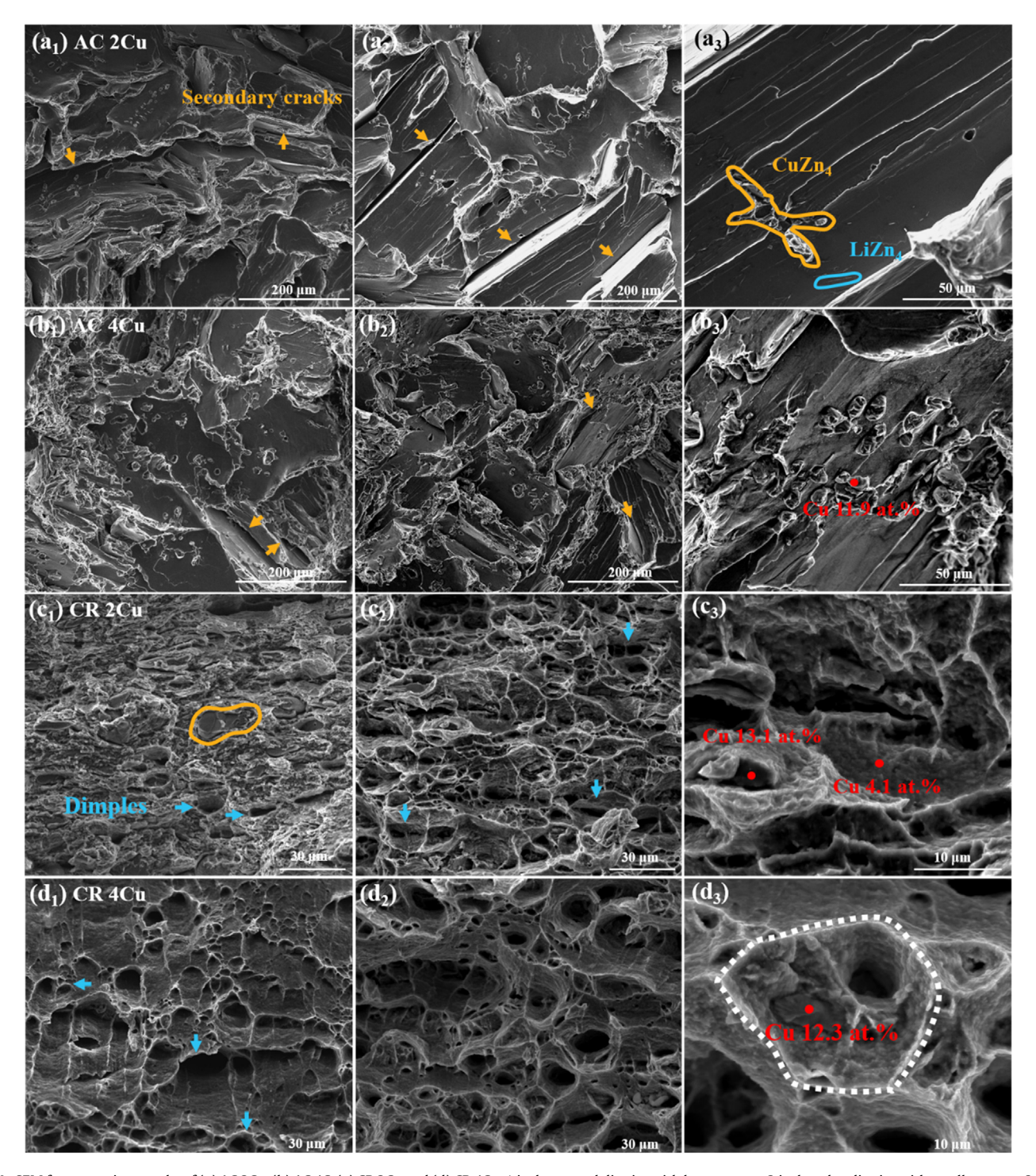


Fig. 4. SEM fracture micrographs of (a) AC 2Cu, (b) AC 4C, (c) CR 2Cu and (d) CR 4Cu. 1 is the central district with larger stress, 2 is the edge district with smaller stress, 3 is the enlarged photograph of 1.

layer, respectively. The proposed equivalent circuits ensure a satisfactory fit to the experimental data, as evidenced by the low values of parameter  $\chi^2$  (in the order of  $10^{-3}$ ) and the fitting lines. Resistance values from EIS fitting results represent the barrier against the migration of ions in association with the corrosion reaction [37]. For both AC and CR alloys, the value of  $R_{ct}$  decreases with the increase of Cu content, indicating the enhancement of electrochemical activity. Conversely, the value of  $R_f$  of 4Cu alloys exceeds that of 2Cu alloys. Besides, the CR alloys exhibit lower  $n_2$  values than AC alloys, which represents a larger deviation of the CPE from

the ideal capacitive behavior. It can be inferred that the CPF formed on the CR alloys has a high degree of surface inhomogeneity or large porosity [38].

#### 3.4. Corrosion rate

The corrosion rate as a function of immersion time is shown in Fig. 6. As a whole, the corrosion rate reveals a decreasing trend with prolonged time. During the first three periods, the corrosion rate decreases rapidly, and then only slightly decreases during

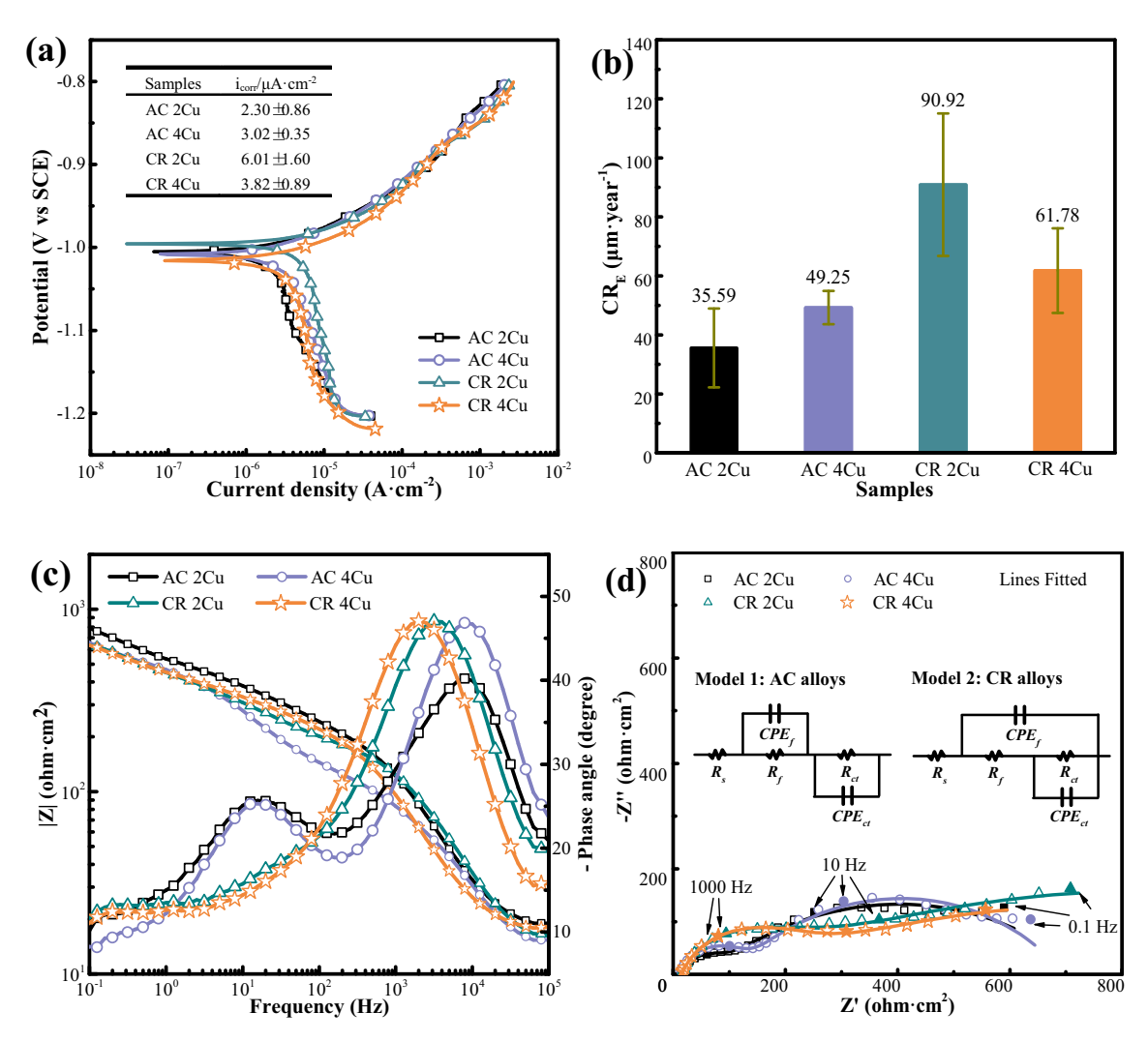


**Fig. 5.** (a) PDP curves, (b) electrochemical corrosion rate, (c) Bode plots, and (d) Nyquist diagrams. The table inserted in Fig. 5a lists the *i<sub>corr</sub>* value obtained from PDP curves. The inserts in Fig. 5d are equivalent circuits for fitting the EIS spectra.

**Table 2**The fitted values of the elements used in the equivalent circuits.

Alloys	$R_s (\Omega \cdot cm^2)$	$\text{CPE}_{\text{f}} \times 10^{\text{-6}}  (\Omega {\cdot} \text{cm}^{-2} {\cdot} \text{s}^{\text{n1}})$	$n_1$	$R_f (\Omega \cdot cm^2)$	$\text{CPE}_{\text{dl}} \times 10^{\text{-4}}  (\Omega {\cdot} \text{cm}^{-2} {\cdot} \text{s}^{\text{n2}})$	$n_2$	$R_{ct} (\Omega \cdot cm^2)$	$\chi^2~(\times 10^{\text{-}3})$
AC 2Cu	15.9	6.17	0.83	59.9	4.77	0.48	665.1	1.6
AC 4Cu	15.9	3.05	0.85	107.0	2.85	0.59	578.3	1.2
CR 2Cu	10.2	4.92	0.81	135.8	10.67	0.29	1366.0	1.3
CR 4Cu	11.6	8.22	0.80	169.5	15.71	0.30	1077.0	1.0

the last two periods. Likewise, the individual data bars of all Zn–Cu–Li alloys display marked height differences during the first three periods (2, 4, and 8 days), and only slight differences during the last two periods (14 and 21 days). This suggests that the surface nature and oxide film stability may have a great influence on corrosion. After immersion for two days, the order of corrosion rate of different alloys is as follows: CR 2Cu > CR 4Cu > AC 4Cu > AC 2Cu, which is consistent with the electrochemical corrosion rate of the bare samples (Fig. 5b). This phenomenon indicates that the initial corrosion is dominated by the surface electrochemical activity. It should be noted that the average corrosion rate of the 4Cu alloys is less than that of the 2Cu alloys after 4 days. Similarly, the CR alloys have a lower corrosion rate at the later stage of immersion (14 days and 21 days) compared with the AC alloys. This suggests that the CPF property effects the corrosion process at the later

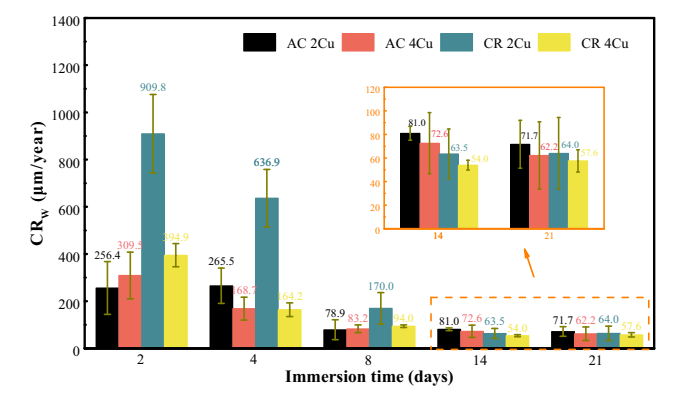


Fig. 6. Corrosion rate of Zn-Cu-Li alloys obtained from the immersion tests.

stage. Thus, the CPF was analyzed in detail to reveal its role in the corrosion process and its effect on corrosion mechanism.

#### 3.5. Corrosion product film analysis

#### 3.5.1. Surface morphology

SEM morphologies of the corrosion products formed on Zn–Cu–Li alloys after immersion in the SBF are shown in Fig. 7. Uneven corrosion occurs on the samples during the initial period. Corrosion products are sparsely distributed on the sample surface. According to the EDS analysis, the globular white cluster in Fig. 7a2 may be Ca-P phase, which is commonly seen as one of the main corrosion products. With the extension of time, the Ca-P products accumulate locally and gradually cover the surface, as seen across the time intervals in Fig. 7. In addition, simonkolleite (Zn<sub>5</sub>(OH)<sub>8</sub>Cl<sub>2</sub>) with Clatomic content of 9.77%, comprised of parallel distributed laminalike subunits (Fig. 7b3) [39], is also detected during immersion. In the enlarged views in Fig. 7c3 and 7c5, cracks in the CPF of CR 2Cu are clearly seen, which is possibly due to inhomogeneous internal stress or dehydration during drying. Moreover, the rolling process has little effect on the CPF morphologies.

#### 3.5.2. Phase compositions

XRD is used to analyze the main phase composition of the CPF after different immersion periods, as shown in Fig. 8. It is worth mentioning that the peak intensity of the corrosion products is much lower than that of the Zn and the CuZn<sub>4</sub> phase, due to the limited amount of corrosion products. The main phase composition of all Zn–Cu–Li alloys includes ZnO/Zn(OH)<sub>2</sub>, CaHPO<sub>4</sub>, and Zn<sub>3</sub>(-PO<sub>4</sub>)<sub>2</sub> after a short immersion period. With increased immersion time, a variety of signals with low intensity are captured in the range of  $10^{\circ}$  to  $40^{\circ}$ , as shown in the detailed view inserted in the figure. These diffraction signals correspond to Zn<sub>5</sub>(OH)<sub>8</sub>Cl<sub>2</sub> and Zn<sub>5</sub>(CO<sub>3</sub>)<sub>2</sub>(OH)<sub>6</sub>. Overall, the variation in CPF phase composition of the 4Cu alloys (Fig. 8b and 8d) is higher than that of the 2Cu alloys (Fig. 8a and 8c). While no compounds containing Cu or Li were detected on the immersed samples, this is likely due to the 5 wt% detection limit of the XRD [37].

To supplement the determination of the phase compositions of the CPFs, XPS results of CR alloys immersed for 2 days and 21 days are shown in Fig. 9. The detailed Cu 2p spectra reveals that the Curelated phases are hard to find in the CPF after 2 days of immersion, and they only appear after a long immersion period. As exhibited in Fig. 9b, the Cu 2p spectra of CR 2Cu is composed of three contributions with maxima at 932.8, 934.6 and 935.6 eV, which corresponds to CuCl<sub>2</sub>, CuO and Cu<sub>2</sub>O, respectively [40–41]. The Curelated phases of CR 4Cu, however, are only made up of CuO, as shown in Fig. 9d. No obvious peaks appear in the binding energy from 53 eV to 58 eV of the Li 1 s spectra due to the limited amount of Li-rich products.

#### 3.5.3. Cross-sectional analysis

Fig. 10 displays the cross-sectional morphologies and corresponding elemental maps of CPFs. The EDS maps in Fig. 10a1 reveal that the Ca and P elements of CPF formed on AC 2Cu surface are distributed in a hierarchical structure, which is a typical phenomenon of Zn and its alloys tested in physiological environment [42–44]. This indicates the continuous evolution process of CPFs, formed by stacking the Ca/P-rich layer and ZnO-rich layer. After 21 days, the delamination of the P element disappears (Fig. 10a2) due to the formation of more Zn<sub>3</sub>(PO<sub>4</sub>)<sub>2</sub> [42]. Meanwhile, 0.6 at.% Cl<sup>-</sup> is found at the shallow pit. The Ca distribution of AC 4Cu immersed for 2 days (Fig. 10b1) is also non-uniform, similar to that of AC 2Cu. After 21 days of immersion, the corrosion of AC 4Cu penetrates the substrate beneath the CPF, as shown in Fig. 10b2.

The matrix with 3.1 at.% Cu content is preferentially corroded, compared with CuZn<sub>4</sub> phase with 12.1 at.% Cu.

In comparison to the AC alloys, the CR alloys show different EDS results and morphologies, as well as different corrosion mechanisms. High Ca and P concentrations in the CPFs of the CR alloys only arise on the outermost surface away from the substrate (Fig. 10c2, 10d1, and 10d2). Besides, the elongated CuZn<sub>4</sub> layer of CR alloys (as confirmed by the laminated structure in Fig. 2a3 and 2b3) acts as a corrosion barrier to block the continuous CPF, eventually leading to the corrosion morphology of "layered ladder". Compared with CR 2Cu, the corrosion of CR 4Cu is more uniform, resulting from the more extended and closely arranged CuZn<sub>4</sub> layers along the rolling direction. This can be roughly verified by the number of CuZn<sub>4</sub> layers of the yellow dotted line arrow in Fig. 2a3 and 2b3. Additionally, Cl is largely enriched in the CPFs of both CR 2Cu and CR 4Cu allovs. For CR 4Cu, most of the Cl is found at the bottom of CPF nearest to the substrate, as shown in Fig. 10d1 and 10d2. For CR 2Cu, however, Cl has occupied almost the whole CPF, as shown in Fig. 10c2.

#### 3.6. Corrosion morphology

Fig. 11 shows the representative SEM images of Zn–Cu–Li alloys after CPF removal to reveal the corrosion mode. The AC alloys have obvious pitting corrosion after 21 days of immersion (marked with red arrows), while the CR alloys exhibit a relatively uniform corrosion behavior without apparent corrosion pits even after a long period of immersion. In particular, residual CuZn<sub>4</sub> particles with around 12.2 at.% Cu are found at the bottom, wall, and surface of the open pits (Fig. 11a5 and 11b5), which is consistent with the corrosion process shown in Fig. 10b2. Some typical preferential corrosion characteristics, however, are observed in both the AC and CR alloys. In Fig. 11a1, the corrosion attack of the phase boundary between CuZn<sub>4</sub> and the matrix or LiZn<sub>4</sub> is clearly visible, marked with blue arrows. As immersion time increases, CuZn<sub>4</sub> is gradually attacked and corroded, as shown in the enlarged image of Fig. 11a4. In addition, preferential corrosion at a triple junction site is also observed (Fig. 11b4). Some shallow pores or grooves appear around or among the CuZn<sub>4</sub> phase (Fig. 11b5, 11c4, 11d3, and 11d5). When the alloys are immersed up to 21 days, dissolution of CuZn<sub>4</sub> phase occurs, as illustrated in Fig. 11c5 and 11d5. The corrosion mode of CR Zn-Cu-Li alloys in the SBF is relatively uniform because uniform corrosion takes place in the grain interior.

#### 3.7. Cell morphology

Fig. 12 depicts the fluorescence staining images of HUVECs with different concentrations of extract media. Both groups of cells in the 100% extract present a round shape. However, when the concentration of extract is reduced to 50% and 10%,the cells exhibit an elongated and spindle-like form, which is considered to be a more healthy cell state than 100% extract group. Particularly, CR 4Cu with higher cell activity significantly enhances cell spreading when compared to CR 2Cu.

#### 4. Discussion

#### 4.1. Corrosion mechanism of Zn-Cu-Li alloys in SBF

When Zn–Cu–Li alloys are immersed in SBF, a thin oxide film composed of ZnO or Zn(OH)<sub>2</sub> is formed on the surface, with anodic, cathodic, and corrosion product formation reactions as follows:

$$Zn \rightarrow Zn^{2+} + 2e^{-} \tag{3}$$

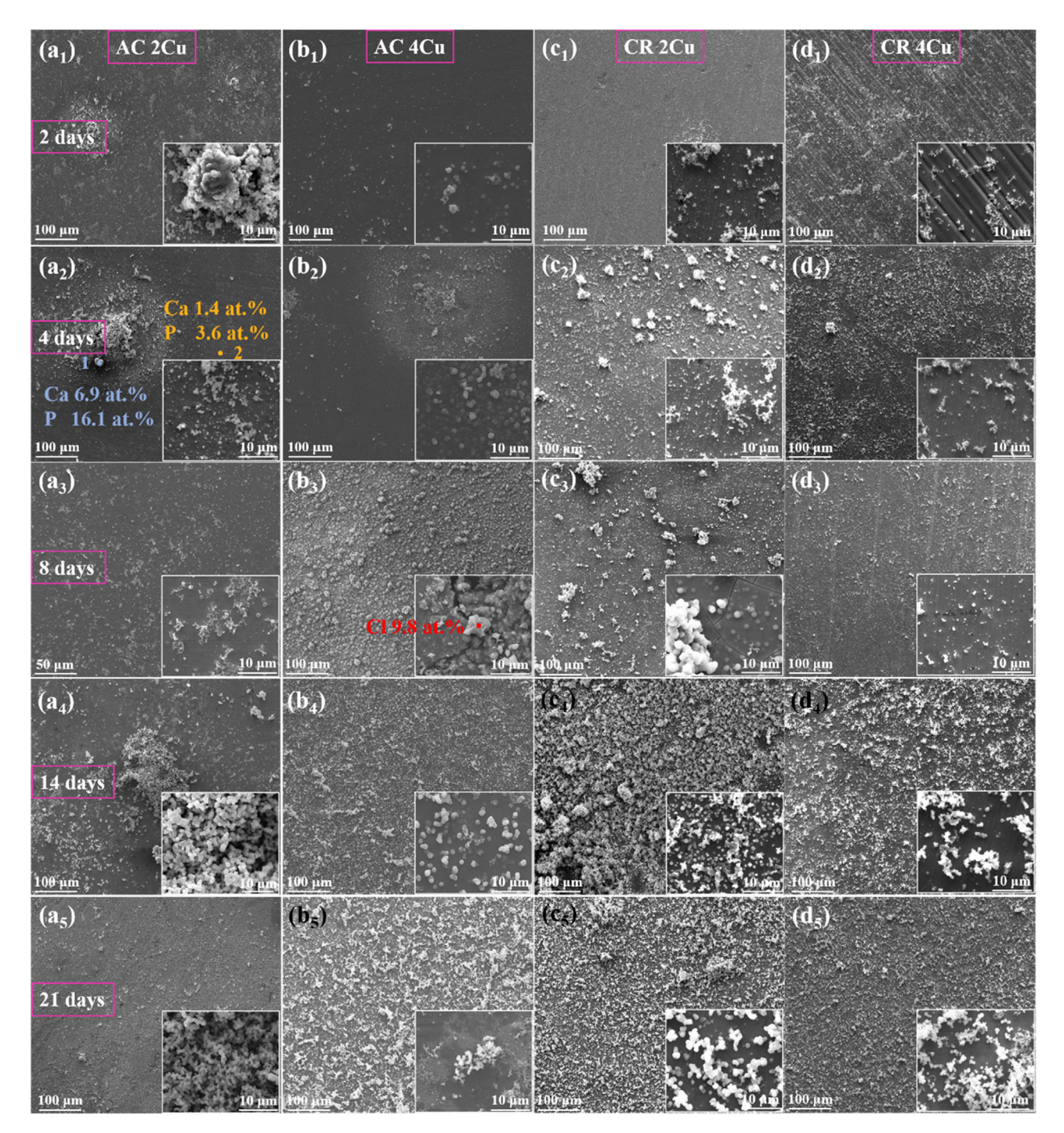


Fig. 7. Surface morphologies of (a) AC 2Cu, (b) AC 4Cu, (c) CR 2Cu, (d) CR 4Cu after immersion in SBF after different days. The insets show local high magnification area.

$$O_2 + 2H_2O + 4e^- \rightarrow 4OH^-$$
 (4)

$$Zn^{2+} + 2OH^- \rightarrow Zn(OH)_2 \tag{5}$$

$$Zn(OH)_2 \rightarrow ZnO + H_2O \tag{6}$$

Meanwhile, the presence of  $Ca^{2+}$  and  $HPO_4^{2-}$  in SBF is beneficial to the formation of new stable  $Zn_3(PO_4)_2$  and Ca/P phases (Eq. (7)), which are specific corrosion products of Zn and its alloys in physiological environment [45–47].

$$Zn^{2+}orCa^{2+} + HPO_4^{2-} \rightarrow Zn_3(PO_4)_2 \text{ or } Ca/P$$
 (7)

Dissolution of Cu promotes the development of CPF consisting of CuO or Cu<sub>2</sub>O, as observed in Fig. 9. In fact, Cu (II) and Cu (I) oxides are typical corrosion products of Cu-contained alloys exposed to saline environment [29,48–49]. In addition, Cl $^{-}$  in SBF, as a reactive species, may produce the formation of some other corrosion products such as CuCl $_2$  [50–51].

$$Cu + O_2 + H_2O + e^- \rightarrow CuOorCu_2O + OH^- \tag{8}$$

$$Cu + 2Cl^- \rightarrow CuCl_2 + 2e^- \tag{9}$$

According to the literature [32,52], the corrosion products of Li in SBF are reported to be LiOH and Li<sub>2</sub>CO<sub>3</sub>, which were not detected

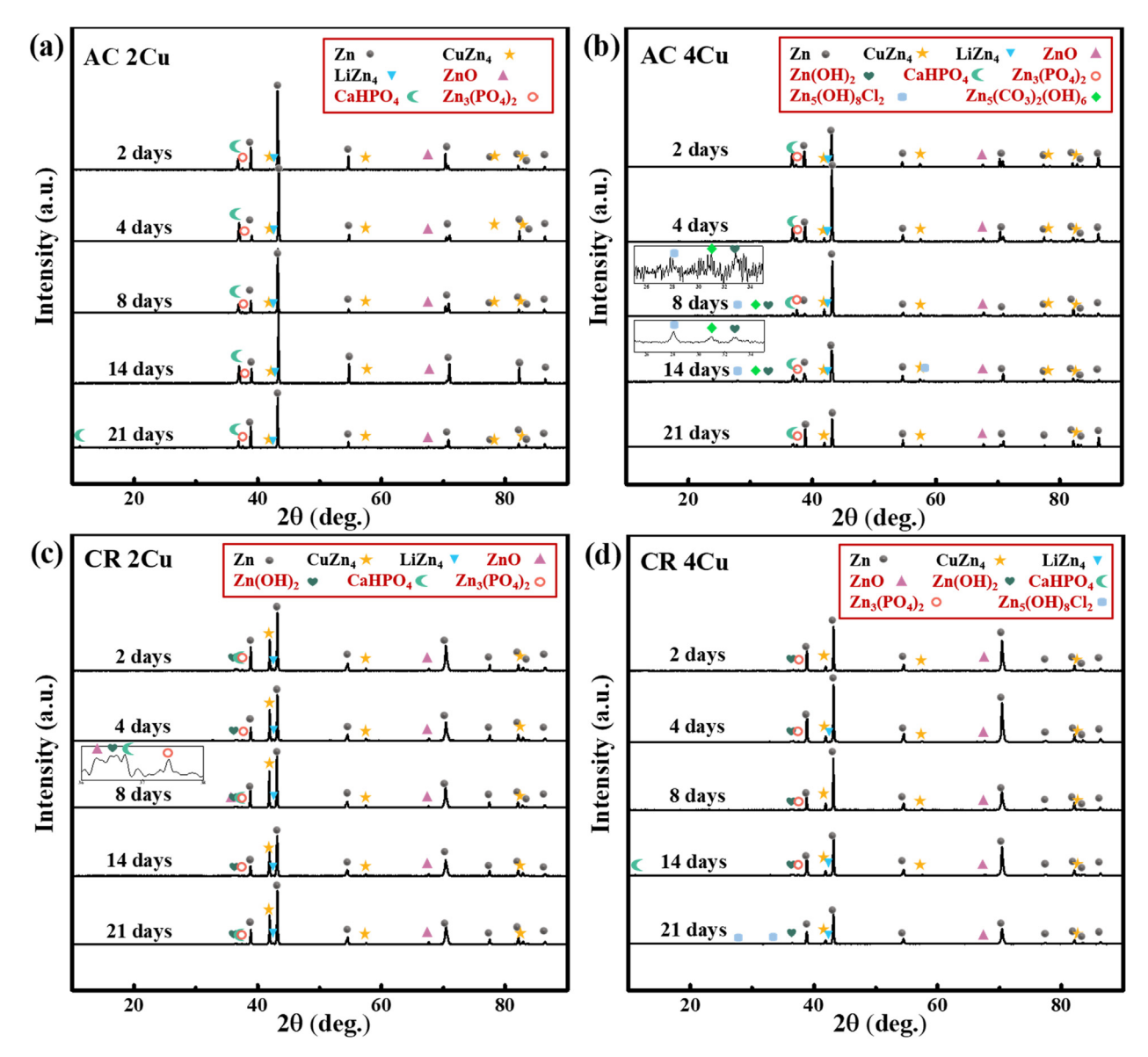


Fig. 8. XRD patterns of the CPFs formed on the Zn-Cu-Li alloys after immersion in SBF for different immersion periods.

in this study due to trace levels.  $Cl^-$  and  $SO_4^{2-}$ , as aggressive species, introduce the possibility of more complex corrosion products, such as  $Zn_5(OH)_8Cl_2$  and  $ZnSO_4$ . Moreover, breakdown of the CPF facilitates the permeation of adsorbed corrosive  $Cl^-$  into the matrix, whose aggregation may induce localized acidification and easily cause local damage, including pits.

Overall, the corrosion of the Zn–Cu–Li alloys in the SBF initiates with preferential corrosion, characterized by some shallow pores and grooves at the phase boundaries, and then evolves into uniform corrosion (Figs. 7, 10, and 11). At the early corrosion stage, phase boundaries (CuZn<sub>4</sub>-matrix) and LiZn<sub>4</sub> with higher activity are clearly damaged after removing the CPF. The galvanic corrosion between the second phase and the matrix with diverse corrosion tendency is the main reason for the occurrence of preferential corrosion sites, which has also been widely reported in other papers [53–56]. After immersion for a longer time, the preferred corrosion sites of the AC alloys show obvious pitting due to the autocatalysis effect (Fig. 10a2, 10b2, 11a5, and 11b5). Subsequently, pits on the AC alloys develop along the depth direction, bypassing the CuZn<sub>4</sub> second phase and seriously corroding the matrix. The small holes or

grooves, however, do not propagate in the depth direction on the CR alloys, because the corrosion is isolated by extended and closely arranged  $\text{CuZn}_4$  layers (Fig. 2a3 and 2b3) with good corrosion resistance. Cross-sectional morphologies in Fig. 10 also validate this claim. An increasing number of holes and grooves generate and merge with adjacent ones, resulting in a relatively uniform corrosion mode. Noticeably, preferential corrosion dominates again after coalescence because sites susceptible to corrosion still exist. Nevertheless, uniform corrosion is the main corrosion trend of CR Zn–Cu–Li alloys in SBF, and the impact of preferential corrosion is weak. Furthermore, compared with the pitting corrosion of pure Zn in SBF [42], the relatively uniform corrosion mode of CR Zn–Cu–Li alloys in the later stage is greatly affected by Cu. Thus, the roles of alloys elements on corrosion behavior need to be further analyzed.

4.2. Influence of Cu content on the corrosion behavior of Zn-Cu-Li alloys

There are two primary forms of Cu atoms in Zn-Cu-Li alloys. One is in the solid solution state in Zn matrix, and the other is in

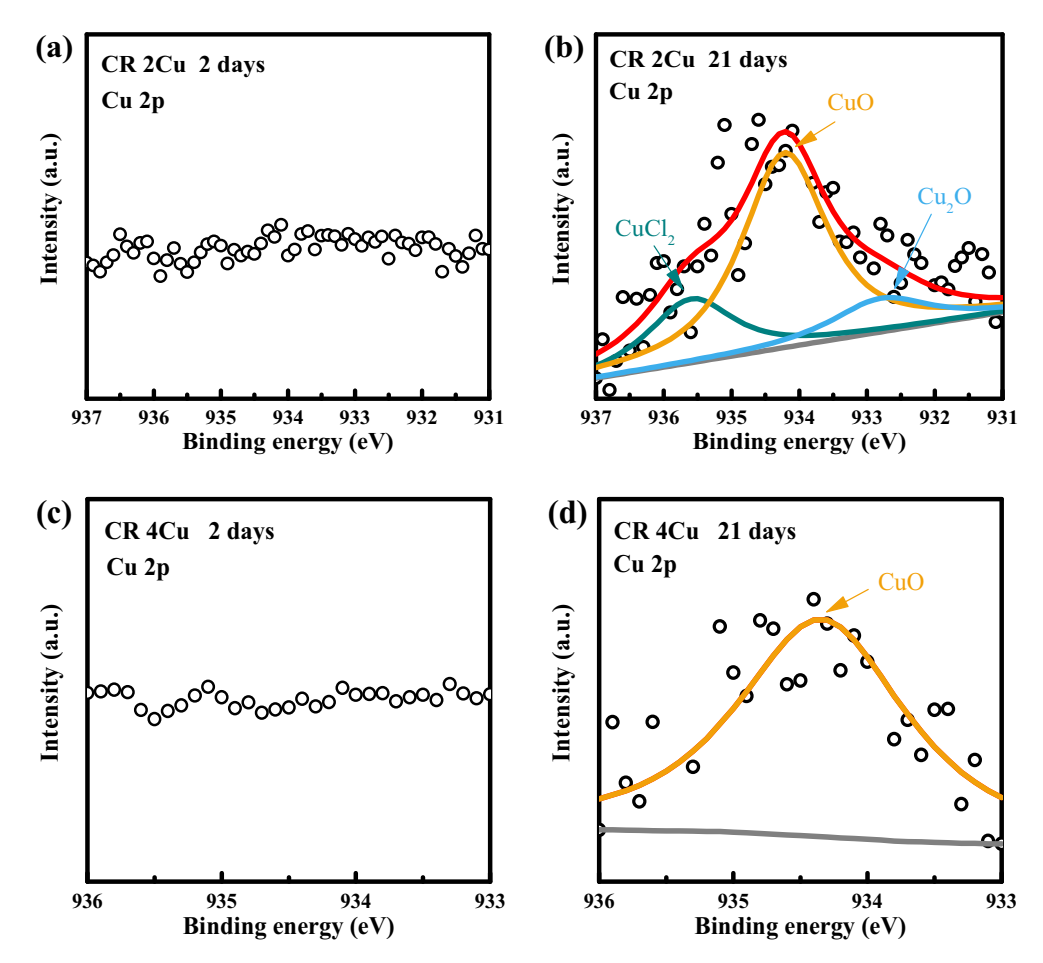


Fig. 9. Cu 2p XPS spectra of CPF for (a-b) CR 2Cu, (c-d) CR 4Cu after immersion in SBF at 2 days and 21 days.

the second phase, CuZn<sub>4</sub>. To compare corrosion tendencies of different microstructures, the surface Volta potential was measured by SKPFM. In general, materials with a high work function (i.e. high Volta potential) show more stable valence electrons, which, because they are restricted to participation in electrochemical reactions, enhance resistance to corrosion attack [57-58]. Fig. 13 displays the surface topography maps with corresponding Volta potential maps of the characteristic structures. In Fig. 13b, Volta potential mapping of CuZn<sub>4</sub> shows a non-uniform distribution, with the bright regions (high Volta potential values) representing  $CuZn_4$ . The potential difference ( $\Delta V$ ) between  $CuZn_4$  and the matrix is about 40 mV. The cross-sectional zone in Fig. 13d shows the same Volta potential law as that in Fig. 13b. Notably, Volta potential value at the phase boundary is remarkably low, thus is more likely to be activated and act as the preferential site for the initiation of localized corrosion. To sum up, the order of discrete Volta potential values is as follows: CuZn₄ > matrix > phase boundary. These large gradients of  $\Delta V$ , in turn, provide the required driving force for galvanic corrosion.

In the early stages of corrosion, solid solution Cu atoms ( $\pm 0.34$  V) heighten the intrinsic standard electrode potential of Zn ( $\pm 0.76$  V). The same changes caused by alloying elements, like Mg and Mn, also exist in other Zn-based alloys [24]. The  $\Delta$ V gradient between CuZn<sub>4</sub> second phase and the matrix (Fig. 13a2), however, leads to the formation of micro-galvanic coupling, which promotes the occurrence of preferential dissolution along the interface of CuZn<sub>4</sub> and the matrix. The galvanic effect of Cu has been widely reported [15,19]. Moreover, the galvanic corrosion is

intensified due to the large amounts of CuZn<sub>4</sub> phase at a higher content of Cu. Therefore, the early corrosion rate (within 2 days) of AC 4Cu is higher than that of AC 2Cu. In the later stages of corrosion, the galvanic corrosion effect is slightly inhibited owning to the formation of CPF on the surface. Importantly, a higher Cu content in the alloys results in a higher proportion of Cu oxides in the CPF, which is confirmed to be CuO and Cu<sub>2</sub>O by XPS (Fig. 9b and 9d). This phenomenon has rarely been mentioned in Zn-Cu alloys studies, but the benefit of CuO and Cu<sub>2</sub>O to CPF is widely accepted by other research [29,48–49]. Thus, it is believed that the presence of CuO and Cu<sub>2</sub>O in CPF of 4Cu alloys can better protect the Zn-Cu-Li matrix from further corrosion. Meanwhile, the extended, consecutive, and closely arranged CuZn<sub>4</sub> layers (Fig. 2a3 and 2b3) exert a prominent corrosion barrier effect due to its high electrochemical resistance, which transforms the corrosion mode from localized corrosion to uniform corrosion. With an increase of Cu content, the interlayer spacing decreases (Fig. 2a3 and 2b3) and the barrier effect increases. Similar phenomenon has also been reported in the study of Liu et al., who found the clear inhibition effect of the second phase and eutectic phase on corrosion [17].

In conclusion, Cu addition has a dual role on the corrosion process of the Zn-based alloy. On one hand, Cu addition accelerates the initial corrosion rate due to the galvanic corrosion between the matrix and CuZn<sub>4</sub> phase. On the other hand, the Cu atoms in the matrix enhances its electrochemical resistance, the laminated CuZn<sub>4</sub> phase provides a physical barrier to corrosion, and the formation of CuO and Cu<sub>2</sub>O in CPF enhances the protection. The two effects are always in competition with each other at different stages.

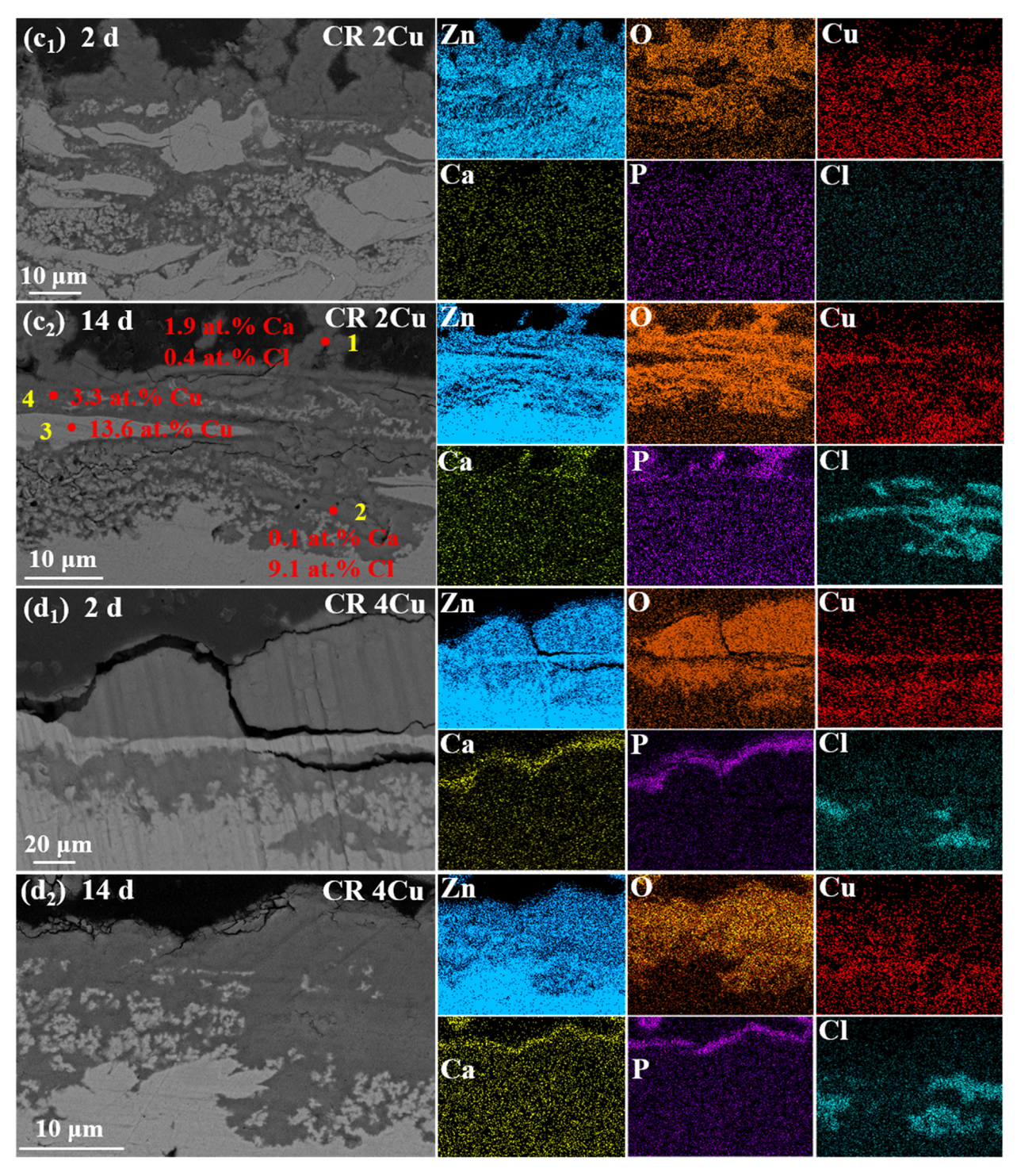


Fig. 10 (continued)

# 4.3. Effects of the rolling process on corrosion resistance and mechanical properties

Two effects of rolling on the corrosion behavior of Zn–Cu–Li alloys are achieved by changing the microstructure. On the one hand, the residual stress of rolling leads to more micro-defects in CR alloys, as reported in the literature [59]. This is responsible for the higher electrochemical activity [60] and higher corrosion

rate of CR alloys in the early stages (Fig. 5b and 6). On the other hand, the rolling process elongates and evenly distributes the large-sized  $CuZn_4$ , forming a laminated corrosion barrier. Such a network barrier not only reduces the corrosion rate in the early stages, but also makes the corrosion more uniform in the later stages. In particular, the corrosion barrier leads to opposite corrosion rate laws of CR and AC alloys in the early stages, that is, CR  $4Cu < CR \ 2Cu \ while \ AC \ 4Cu > AC \ 2Cu.$  The same phenomenon

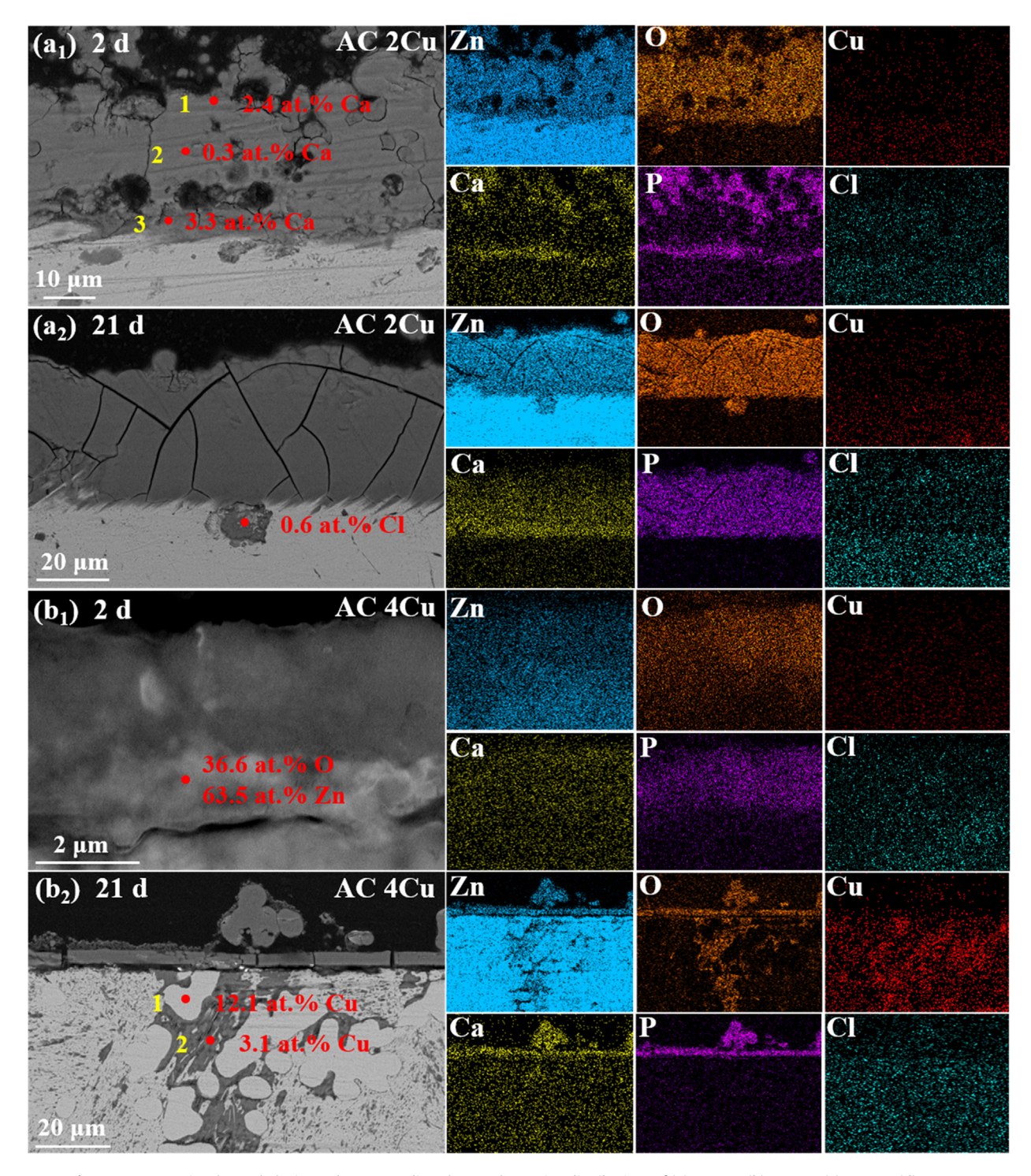


Fig. 10. Cross-sectional morphologies and corresponding elemental mapping distributions of (a) AC 2Cu, (b) AC 4Cu, (c) CR 2Cu, (d) CR 4Cu.

can be extrapolated to other Zn-based alloys, such as Zn-Mg [61], whose second phase possesses large size or good corrosion resistance.

The mechanical properties of Zn–Cu–Li alloys are markedly increased (about 2-fold *UTS* and 80-fold *E* in Fig. 3) through rolling. Rolling refines the grain significantly and regulates the distribution and shape of the second phase. The refined grain size in the ternary

alloys further improves the strength by grain boundary strengthening, as described by the Hall-Petch relationship [54,62]. Also, the lower E values of AC Zn–Cu–Li alloys are likely due to the existence of coarse CuZn<sub>4</sub> phases [24,54], which act as crack nucleation sites, as shown in Fig. 4a3 and 4b3. The rolling process, however, ameliorates the shape of CuZn<sub>4</sub> and the coherent relationship between CuZn<sub>4</sub> and the matrix, further contributing to deforma-

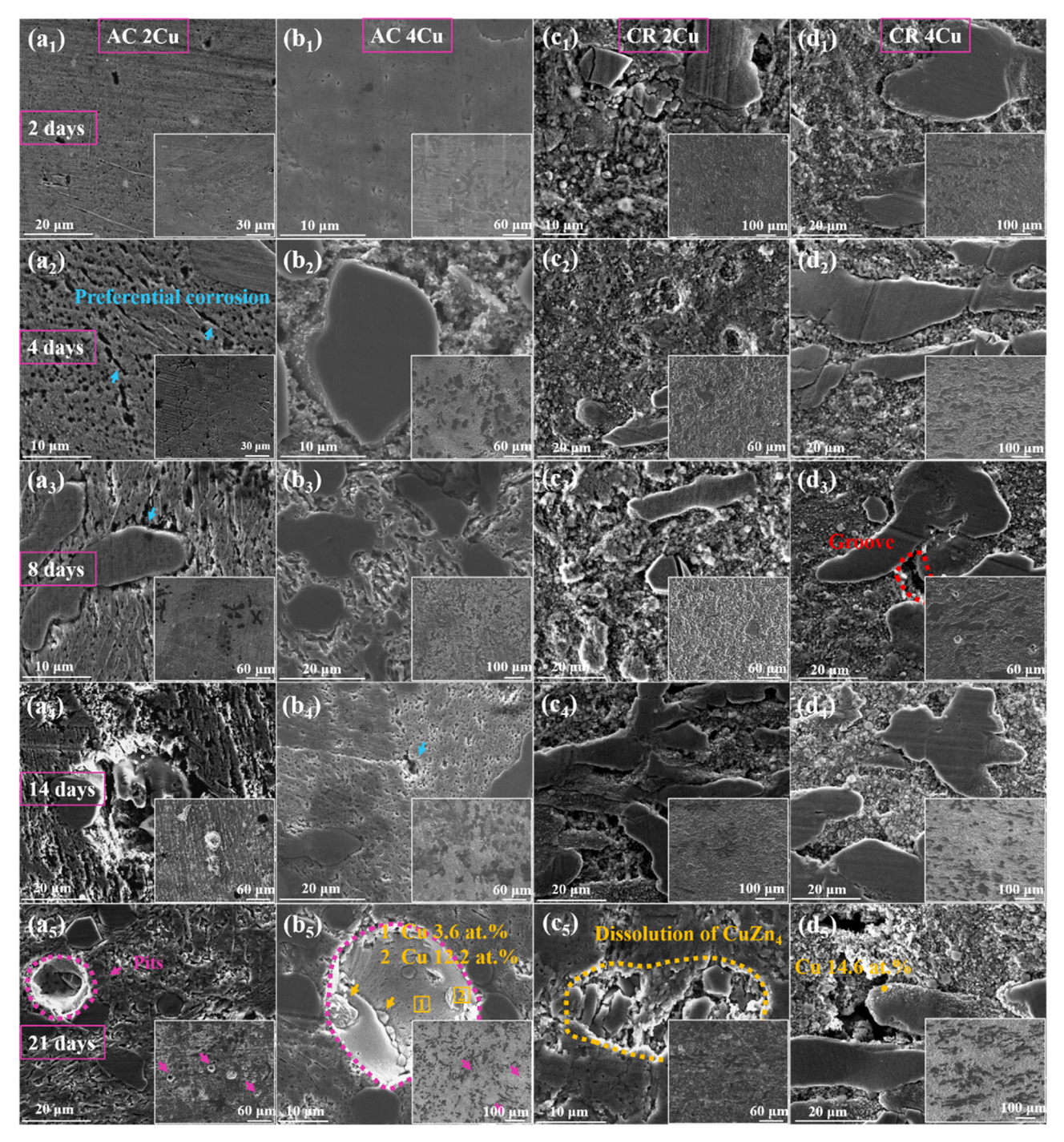


Fig. 11. Surface morphologies of (a) AC 2Cu, (b) AC 4Cu, (c) CR 2Cu, (d) CR 4Cu immersed in SBF for (1) 2 days, (2) 4 days, (3) 8 days, (4) 14 days, (5) 21 days after removal of CPF.

tion uniformity and plasticity. The observed tight connection between  $\text{CuZn}_4$  and the matrix in Fig. 4c3 and 4d3 provides clear evidence for this. Overall, the rolling process significantly improves the mechanical properties in terms of changing the microstructure.

Table 3 presents the mechanical properties of the tested alloys in comparison to those of Zn–Cu–X ternary alloys for biological use. Some alloys possess *UTS* of 328–482 MPa but *E* of 0.9–4.8% [8,63] and the resulting brittleness hinders medical application.

On the contrary, alloys with *UTS* of 202–284 MPa and *E* of 19.6–75.2% [16,19,26,45,64] provide a relatively good combination of strength and plasticity. Judging from the mechanical properties, in this paper, 2Cu and 4Cu alloys with *UTS* > 300 MPa and E > 15% exhibit sufficient tensile and deformation capacity. Combined with the degradation behavior discussed above, Zn–2Cu–0.02Li and Zn–4Cu–0.02Li seems to be good candidates for designing biodegradable implants.

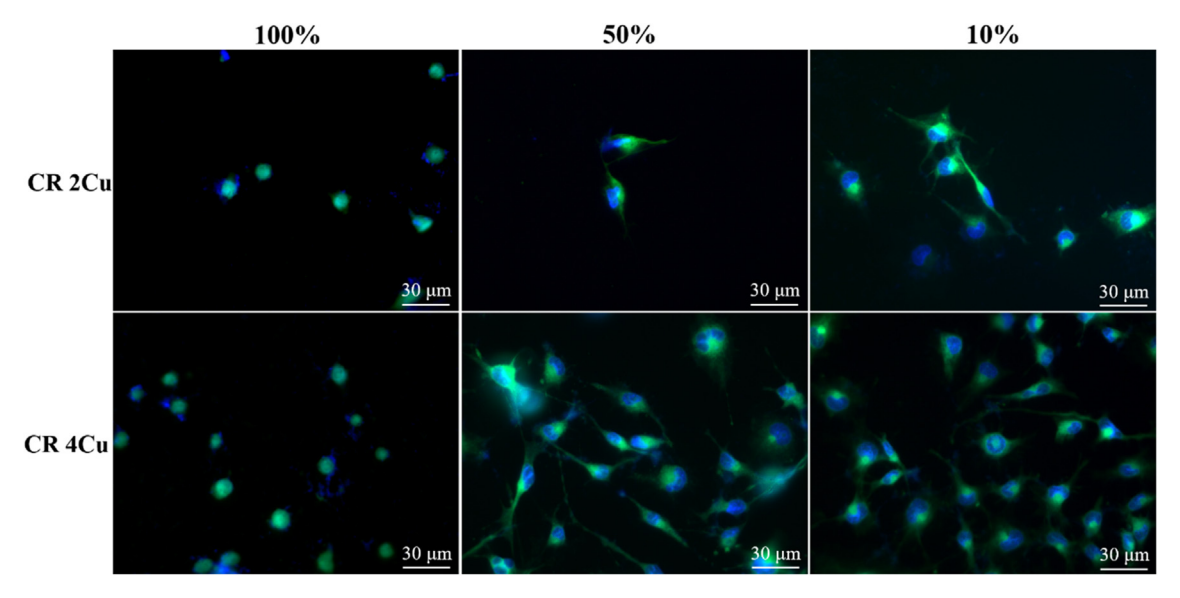


Fig. 12. LSCM images of HUVECs. The cytoplasm (green) and nucleus (blue) were counterstained. (For interpretation of the references to colour in this figure legend, the reader is referred to the web version of this article.)

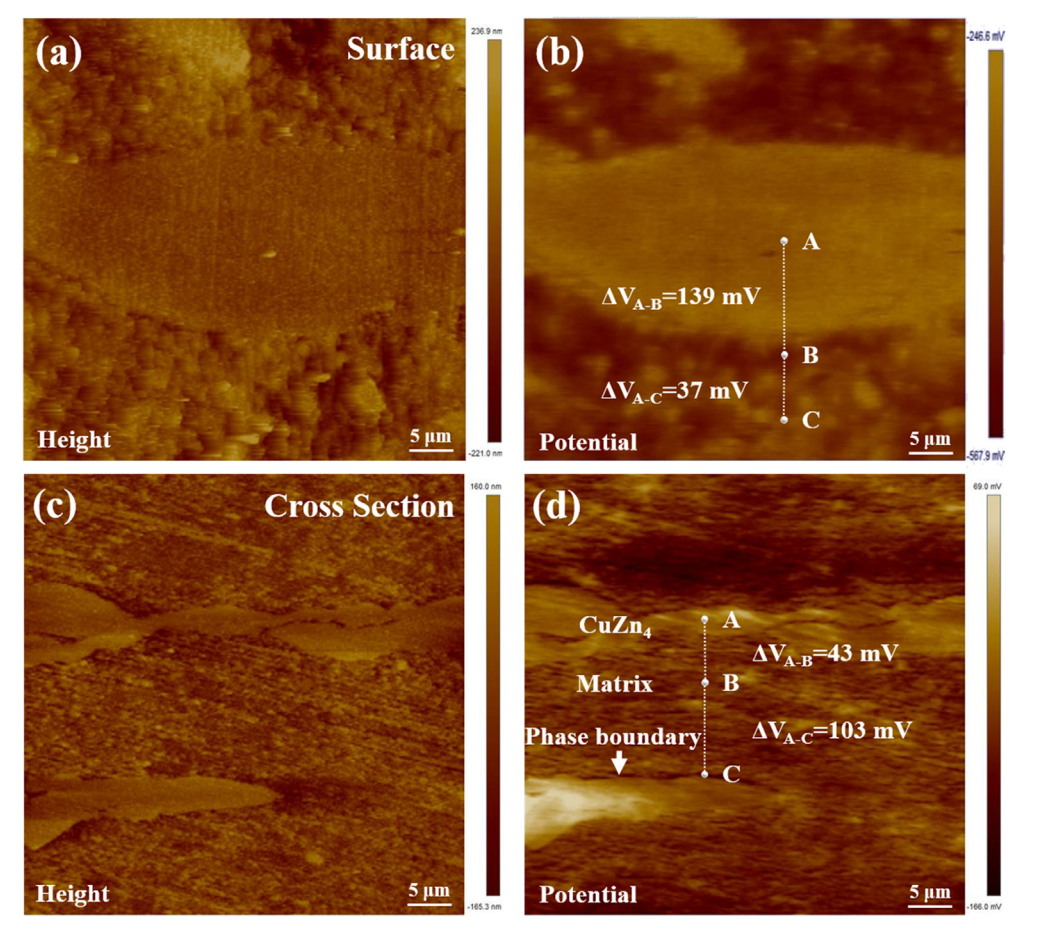


Fig. 13. (a, c) Topography and (b, d) Volta potential of CuZn4 in Zn-Cu-Li alloys.

**Table 3**Mechanical properties of studied alloys and reported Zn–Cu–X alloys.

Alloys	States	YS (MPa)	UTS (MPa)	E (%)	Article
Zn-2Cu-0.02Li	Cold rolling	254	352	49.1	Our study
Zn-4Cu-0.02Li	Cold rolling	256	342	39.8	
Zn-2Cu-0.05Ti	As cast	259	482	2.5	[63]
Zn-2Cu-0.1Ti		162	328	1.8	
Zn-1Cu-0.1Ti	Cold rolling	204	250	75.2	[16]
Zn-3Cu-0.2Ti	Cold rolling	211	271	72.1	[64]
Zn-1.5Cu-1.5Ag	Extrusion	162	220	44.1	[19]
Zn-3Cu-0.1Mg	Extrusion	346	365	4.8	[8]
Zn-3Cu-0.5Mg		403	416	1.9	
Zn-3Cu-1Mg		427	441	0.9	
Zn-0.5Cu-0.2Fe	Extrusion	152	202	41.2	[45]
Zn-0.5Cu-0.4Fe		182	240	20.5	
Zn-3Cu-0.5Fe	Extrusion	231	284	32.7	[26]
Zn-3Cu-1Fe		221	272	19.6	

#### 5. Conclusions

In the present work, two aspects of the corrosion behavior of Zn-based alloys in SBF was analyzed, Cu content and rolling process. The principal conclusions are as follows:

- (1) The cold-rolled Zn-4Cu-0.02Li is a potential biodegradable implant material from the perspective of corrosion behavior and mechanical properties. This sample exhibited the highest tensile properties, with a yield strength of 256 MPa, an ultimate strength of 342 MPa, and a fracture elongation of 39.8%. The corrosion rate of Zn-4Cu-0.02Li after immersion in SBF for 21 days was about 55 μm/year.
- (2) The corrosion mechanisms of as-cast and cold-rolled alloys showed discrepancy. Both alloys were initially corroded at preferential sites such as phase boundaries and LiZn<sub>4</sub> second phase. At the later stages of immersion, the as-cast alloy presented severe localized corrosion, while the corrosion mode of cold-rolled alloy was transformed to uniform corrosion.
- (3) Cu has a quadruple effect on the corrosion behavior of Zn in SBF: changing the intrinsic potential, producing galvanic corrosion, increasing the corrosion resistance of corrosion products, and acting as a barrier to corrosion. After immersion for a period of time, the protective effect of Cu on corrosion was enhanced with the increasing Cu content.
- (4) Rolling was beneficial to the corrosion resistance and mechanical properties of the Zn alloy. Although microdefects were added, rolling improved the shape of CuZn<sub>4</sub> second phase, resulting in a uniform corrosion mode. Moreover, rolling significantly enhanced the mechanical strength by improving the deformation incongruity between the matrix and CuZn<sub>4</sub>.

#### 6. Data availability statement

The raw/processed data required to reproduce these findings cannot be shared at this time as the data is related to an ongoing study.

#### **Declaration of Competing Interest**

The authors declare that they have no known competing financial interests or personal relationships that could have appeared to influence the work reported in this paper.

#### Acknowledgement

This work was supported by the National Natural Science of China (Grants No. and No.) and Guangdong Major Project of Basic and Applied Basic Research (No.).

#### References

- [1] Y. Liu, Y. Zheng, X.-H. Chen, J.-A. Yang, H. Pan, D. Chen, L. Wang, J. Zhang, D. Zhu, S. Wu, K.W.K. Yeung, R.-C. Zeng, Y. Han, S. Guan, Fundamental theory of biodegradable metals-definition, criteria, and design, Adv. Funct. Mater. 29 (18) (2019) 1805402, https://doi.org/10.1002/adfm.v29.1810.1002/adfm.201805402.
- [2] P.K. Bowen, J. Drelich, J. Goldman, Zinc exhibits ideal physiological corrosion behavior for bioabsorbable stents, Adv. Mater. 25 (18) (2013) 2577–2582.
- [3] H. Kabir, K. Munir, C.E. Wen, et al., Recent research and progress of biodegradable zinc alloys and composites for biomedical applications: Biomechanical and biocorrosion perspectives, Bioact. Mater. 6 (2021) 836– 879
- [4] S. Zhu, C. Wu, G. Li, Y. Zheng, J.-F. Nie, Microstructure, mechanical properties and creep behaviour of extruded Zn-xLi (x= 0.1, 0.3 and 0.4) alloys for biodegradable vascular stent applications, Mater. Sci. Eng. A 777 (2020) 139082, https://doi.org/10.1016/j.msea.2020.139082.
- [5] H.F. Li, Z.Z. Shi, L.N. Wang, Opportunities and challenges of biodegradable Zn-based alloys, J. Mater. Sci. Technol. 46 (2020) 136–138.
- [6] X. Qu, H. Yang, B.o. Jia, Z. Yu, Y. Zheng, K. Dai, Biodegradable Zn-Cu alloys show antibacterial activity against MRSA bone infection by inhibiting pathogen adhesion and biofilm formation, Acta Biomater. 117 (2020) 400-417.
- [7] Z. Tang, J. Niu, H. Huang, H. Zhang, J. Pei, J. Ou, G. Yuan, Potential biodegradable Zn-Cu binary alloys developed for cardiovascular implant applications, J. Mech. Behav. Biomed. 72 (2017) 182–191.
- [8] Z. Tang, H. Huang, J. Niu, L. Zhang, H. Zhang, J. Pei, J. Tan, G. Yuan, Design and characterizations of novel biodegradable Zn-Cu-Mg alloys for potential biodegradable implants, Mater. Design 117 (2017) 84–94.
- [9] H. Guo, D. Xia, Y. Zheng, Y. Zhu, Y. Liu, Y. Zhou, A pure zinc membrane with degradability and osteogenesis promotion for guided bone regeneration: In vitro and in vivo studies, Acta Biomater. 106 (2020) 396–409.
- [10] M. Watroba, W. Bednarczyk, J. Kawałko, K. Mech, M. Marciszko, G. Boelter, M. Banzhaf, P. Bała, Design of novel Zn-Ag-Zr alloy with enhanced strength as a potential biodegradable implant material, Mater. Des. 183 (2019) 108154, https://doi.org/10.1016/j.matdes.2019.108154.
- [11] W. Yuan, D. Xia, S. Wu, Y. Zheng, Z. Guan, J.V. Rau, A review on current research status of the surface modification of Zn-based biodegradable metals, Bioact. Mater. 7 (2022) 192–216.
- [12] M. Ashuri, F. Moztarzadeh, N. Nezafati, A. Ansari Hamedani, M. Tahriri, Development of a composite based on hydroxyapatite and magnesium and zinc-containing sol-gel-derived bioactive glass for bone substitute applications, Mater. Sci. Eng. C 32 (8) (2012) 2330–2339.
- [13] M. Abdel-Hady Gepreel, M. Niinomi, Biocompatibility of Ti-alloys for long-term implantation, J. Mech. Behav. Biomed. 20 (2013) 407–415.
- [14] N. Yang, N. Balasubramani, J. Venezuela, S. Almathami, C. Wen, M. Dargusch, The influence of Ca and Cu additions on the microstructure, mechanical and degradation properties of Zn–Ca–Cu alloys for absorbable wound closure device applications, Bioact. Mater. 6 (5) (2021) 1436–1451.
- [15] C. Shuai, Z. Dong, C. He, W. Yang, S. Peng, Y. Yang, F. Qi, A peritectic phase refines the microstructure and enhances Zn implants, J. Mater. Res. Technol. 9 (3) (2020) 2623–2634.

- [16] J. Lin, X. Tong, Z. Shi, D. Zhang, L. Zhang, K. Wang, A. Wei, L. Jin, J. Lin, Y. Li, C. Wen, A biodegradable Zn-1Cu-0.1Ti alloy with antibacterial properties for orthopedic applications, Acta Biomater. 106 (2020) 410-427.
- [17] J. Lin, X. Tong, Q. Sun, Y. Luan, D. Zhang, Z. Shi, K. Wang, J. Lin, Y. Li, M. Dargusch, C. Wen, Biodegradable ternary Zn-3Ge-0.5X (X=Cu, Mg, and Fe) alloys for orthopedic applications, Acta Biomater. 115 (2020) 432-446.
- [18] P. Li, W. Zhang, J. Dai, A.B. Xepapadeas, E. Schweizer, D. Alexander, L. Scheideler, C. Zhou, H. Zhang, G. Wan, J. Geis-Gerstorfer, Investigation of zinccopper alloys as potential materials for craniomaxillofacial osteosynthesis implants, Mater. Sci. Eng. C 103 (2019) 109826, https://doi.org/10.1016/j. msec.2019.109826.
- [19] C. Chen, R. Yue, J. Zhang, H. Huang, J. Niu, G. Yuan, Biodegradable Zn-1.5Cu-1.5Ag alloy with anti-aging ability and strain hardening behavior for cardiovascular stents, Mater. Sci. Eng. C 116 (2020) 111172, https://doi.org/ 10.1016/j.msec.2020.111172.
- [20] C. Zhou, H.F. Li, Y.X. Yin, et al., Long-term in vivo study of biodegradable Zn-Cu stent: A 2-year implantation evaluation in porcine coronary artery, Acta Biomater. 97 (2019) 657-670.
- [21] C. Shen, X. Liu, B.o. Fan, P. Lan, F. Zhou, X. Li, H. Wang, X. Xiao, L.i. Li, S. Zhao, Z. Guo, Z. Pu, Y. Zheng, Mechanical properties, in vitro degradation behavior, hemocompatibility and cytotoxicity evaluation of Zn-1.2Mg alloy for biodegradable implants, RSC Adv. 6 (89) (2016) 86410-86419.
- [22] X. Liu, J. Sun, Y. Yang, F. Zhou, Z. Pu, L.i. Li, Y. Zheng, Microstructure, mechanical properties, in vitro degradation behavior and hemocompatibility of novel Zn-Mg-Sr alloys as biodegradable metals, Mater. Lett. 162 (2016) 242–245.
- [23] H. Gong, K. Wang, R. Strich, J.G. Zhou, In vitro biodegradation behavior, mechanical properties, and cytotoxicity of biodegradable Zn-Mg alloy, J. Biomed. Mater. Res. B 103 (8) (2015) 1632-1640.
- [24] X. Liu, J. Sun, F. Zhou, Y. Yang, R. Chang, K. Qiu, Z. Pu, L.i. Li, Y. Zheng, Microalloying with Mn in Zn-Mg alloy for future biodegradable metals application, Mater. Design 94 (2016) 95–104.
- [25] M.S. Dambatta, S. Izman, D. Kurniawan, H. Hermawan, Processing of Zn-3Mg alloy by equal channel angular pressing for biodegradable metal implants, J. King Saud Univ. Sci. 29 (4) (2017) 455-461.
- [26] R. Yue, H. Huang, G. Ke, H. Zhang, J. Pei, G. Xue, G. Yuan, Microstructure, mechanical properties and in vitro degradation behavior of novel Zn-Cu-Fe alloys, Mater. Charact. 134 (2017) 114–122.
- [27] B.L. Jiang, T. Guo, Q.J. Peng, et al., Proton irradiation effects on the electron work function, corrosion and hardness of austenitic stainless steel phase, Corros. Sci. 157 (2019) 498-507.
- [28] Z.X. Ma, X.L. Xiong, L.N. Zhang, Z.H. Zhang, Y. Yan, Y.J. Su, Experimental study on the diffusion of hydrogen along individual grain boundaries in nickel, Electrochem. Commun. 92 (2018) 24–28.
- [29] W. Wu, Z. Dai, Z. Liu, C. Liu, X. Li, Synergy of Cu and Sb to enhance the resistance of 3%Ni weathering steel to marine atmospheric corrosion, Corros. Sci. 183 (2021) 109353, https://doi.org/10.1016/j.corsci.2021.109353.
- [30] Z.Z. Shi, X.X. Gao, H.J. Zhang, et al., Design biodegradable Zn alloys: Second phases and their significant influences on alloy properties, Bioact. Mater. 5 (2020) 210–218.
- [31] E. Mostaed, M. Sikora-Jsinska, J.W. Drelich, et al., Zinc-based alloys for degradable vascular stent applications, Acta Biomater. 71 (2018) 1-23.
- [32] Z. Li, Z.-Z. Shi, Y. Hao, H.-F. Li, H.-J. Zhang, X.-F. Liu, L.-N. Wang, Insight into role and mechanism of Li on the key aspects of biodegradable Zn-Li alloys: Microstructure evolution, mechanical properties, corrosion behavior and cytotoxicity, Mater. Sci. Eng. C 114 (2020) 111049, https://doi.org/10.1016/j. msec.2020.111049.
- [33] J. Venezuela, M.S. Dargusch, The influence of alloying and fabrication on the mechanical properties, biodegradability techniques biocompatibility of zinc: a comprehensive review, Acta Biomater. 87 (2019)
- [34] Z.Z. Shi, J. Yu, X.F. Liu, Microalloyed Zn-Mn alloys: From extremely brittle to
- extraordinarily ductile at room temperature, Mater. Des. 144 (2018) 343–352. [35] Y. Meng, L. Liu, D. Zhang, C. Dong, Y.u. Yan, A.A. Volinsky, L.-N. Wang, Initial formation of corrosion products on pure zinc in saline solution, Bioact, Mater. 4 (2019) 87-96.
- [36] W.R. Osório, C. Brito, L.C. Peixoto, A. Garcia, Electrochemical behavior of Znrich Zn-Cu peritectic alloys affected by macrosegregation and microstructural array, Electrochim. Acta 76 (2012) 218-228.
- [37] W. Wu, Z. Liu, Q. Wang, X. Li, Improving the resistance of high-strength steel to SCC in a SO<sub>2</sub>-polluted marine atmosphere through Nb and Sb microalloying, Corros. Sci. 170 (2020) 108693, https://doi.org/10.1016/j.corsci.2020.108693.
- [38] W. Wu, X. Cheng, J. Zhao, X. Li, Benefit of the corrosion product film formed on a new weathering steel containing 3% nickel under marine atmosphere in Maldives, Corros. Sci. 165 (2020) 108416, https://doi.org/10.1016/ j.corsci.2019.108416.
- [39] M.M. Alves, L.M. Marques, I. Nogueira, C.F. Santos, S.B. Salazar, S. Eugénio, N.P. Mira, M.F. Montemor, In silico, in vitro and antifungal activity of the surface layers formed on zinc during this biomaterial degradation, Appl. Surf. Sci. 447 (2018) 401-407.

- [40] NIST XPS database. <a href="https://srdata.nist.gov/xps/selEnergyType.aspx">https://srdata.nist.gov/xps/selEnergyType.aspx</a>.
   [41] W. Wu, Q. Wang, L. Yang, Z. Liu, X. Li, Y. Li, Corrosion and SCC initiation behavior of low-alloy high-strength steels microalloyed with Nb and Sb in a simulated polluted marine atmosphere, J. Mater. Res. Technol. 9 (6) (2020) 12976-12995
- [42] S. Huang, W. Wu, Y. Su, L. Qiao, Y.u. Yan, Insight into the corrosion behaviour and degradation mechanism of pure zinc in simulated body fluid, Corros. Sci. 178 (2021) 109071, https://doi.org/10.1016/j.corsci.2020.109071.
- [43] H. Yang, X. Qu, W. Lin, C. Wang, D. Zhu, K. Dai, Y. Zheng, In vitro and in vivo studies on zinc-hydroxyapatite composites as novel biodegradable metal matrix composite for orthopedic applications, Acta Biomater. 71 (2018) 200-214.
- [44] S. Zhao, J.M. Seitz, R. Eifler, et al., Zn-Li alloy after extrusion and drawing: structural, mechanical characterization, and biodegradation in abdominal aorta of rat, Mater. Sci. Eng. C 76 (2017) 301-312.
- [45] W. Zhang, P. Li, G. Shen, X. Mo, C. Zhou, D. Alexander, F. Rupp, J. Geis-Gerstorfer, H. Zhang, G. Wan, Appropriately adapted properties of hotextruded Zn-0.5Cu-xFe alloys aimed for biodegradable guided bone regeneration membrane application, Bioact. Mater. 6 (4) (2021) 975-989.
- [46] B. Jia, H.T. Yang, Z.C. Zhang, et al., Biodegradable Zn-Sr alloy for bone regeneration in rat femoral condyle defect model: In vitro and in vivo studies, Bioact. Mater. 6 (2021) 1588-1604.
- [47] S. Huang, L. Chen, B. Jiang, L. Qiao, Y.u. Yan, Early electrochemical characteristics and corrosion behaviors of pure zinc in simulated body fluid, Electroanal. Chem. 886 (2021) 115145, https://doi.org/10.1016/ .jelechem.2021.115145
- [48] M. Metikoš-Huković, I. Škugor, Z. Grubač, R. Babić, Complexities of corrosion behaviour of copper-nickel alloys under liquid impingement conditions in saline water, Electrochim. Acta 55 (9) (2010) 3123-3129.
- [49] D.C. Kong, C.F. Dong, Z.R. Zheng, et al., Surface monitoring for pitting evolution into uniform corrosion on Cu-Ni-Zn ternary alloy in alkaline chloride solution: ex-situ LCM and in-situ SECM, Appl. Surf. Sci. 440 (2018) 245-257.
- [50] J. Luo, C. Hein, J.-F. Pierson, F. Mücklich, Localised corrosion attacks and oxide growth on copper in phosphate-buffered saline, Mater. Charact. 158 (2019) 109985, https://doi.org/10.1016/j.matchar.2019.109985.
- [51] T. Kosec, Z. Qin, J. Chen, et al., Copper corrosion in bentonite/saline groundwater solution: Effects of solution and bentonite chemistry, Corros. Sci. 90 (2015) 248-258.
- [52] R.-C. Zeng, L.u. Sun, Y.-F. Zheng, H.-Z. Cui, E.-H. Han, Corrosion and characterisation of dual phase Mg-Li-Ca alloy in Hank's solution: the influence of microstructural features, Corros. Sci. 79 (2014) 69-82.
- [53] X.W. Liu, J.K. Sun, K.J. Qiu, et al., Effects of alloying elements (Ca and Sr) on microstructure, mechanical property and in vitro corrosion behavior of biodegradable Zn-1.5Mg alloy, J. Alloy. Compd. 664 (2016) 444-452.
- [54] J. Young, R.G. Reddy, Synthesis, mechanical properties, and in vitro corrosion behavior of biodegradable Zn-Li-Cu alloys, J. Alloy. Compd. 844 (2020) 156257.
- [55] Z.-Z. Shi, J. Yu, X.-F. Liu, L.-N. Wang, Fabrication and characterization of novel biodegradable Zn-Mn-Cu alloys, J. Mater. Sci. Technol. 34 (6) (2018) 1008-
- [56] P.K. Bowen, J.-M. Seitz, R.J. Guillory, J.P. Braykovich, S. Zhao, J. Goldman, J.W. Drelich, Evaluation of wrought Zn-Al alloys (1, 3, and 5 wt % Al) through mechanical and in vivo testing for stent applications, J. Biomed. Mater. Res. B 106 (1) (2018) 245-258.
- [57] E. Rahimi, A. Rafsanjani-Abbasi, A. Imani, S. Hosseinpour, A. Davoodi, Correlation of surface Volta potential with galvanic corrosion initiation sites in solid-state welded Ti-Cu bimetal using AFM-SKPFM, Corros. Sci. 140 (2018) 30-39.
- [58] C. Örnek, D.L. Engelberg, SKPFM measured Volta potential correlated with strain localisation in microstructure to understand corrosion susceptibility of cold-rolled grade 2205 duplex stainless steel, Corros. Sci. 99 (2015) 164-171.
- [59] C. Wang, Z. Yu, Y. Cui, Y. Zhang, S. Yu, G. Qu, H. Gong, Processing of a novel Zn alloy micro-tube for biodegradable vascular stent application, J. Mater. Sci. Technol. 32 (9) (2016) 925–929.
- [60] G. Ma, G. Wu, W. Shi, S. Xiang, Q. Chen, X. Mao, Effect of cold rolling on the corrosion behavior of Ta-4W alloy in sulphuric acid, Corros. Sci. 176 (2020) 108924, https://doi.org/10.1016/j.corsci.2020.108924.
- E. Mostaed, M. Sikora-Jsinska, A. Mostaed, et al., Novel Zn-based alloys for biodegradable stent applications: Design, development and in vitro degradation, J. Mech. Behav. Biomed. 60 (2016) 581–602.
- [62] A. Jarzębska, M. Bieda, J. Kawałko, Ł. Rogal, P. Koprowski, K. Sztwiertnia, W. Pachla, M. Kulczyk, A new approach to plastic deformation of biodegradable zinc alloy with magnesium and its effect on microstructure and mechanical properties, Mater. Lett. 211 (2018) 58-61.
- [63] L. Zhang, X.Y. Liu, H. Huang, et al., Effect of Ti on microstructure, mechanical properties and biodegradable behavior of Zn-Cu alloy, Mater. Lett. 244 (2019) 119\_122
- [64] J. Lin, X. Tong, K. Wang, Z. Shi, Y. Li, M. Dargusch, C. Wen, Biodegradable Zn-3Cu and Zn-3Cu-0.2Ti alloys with ultrahigh ductility and antibacterial ability for orthopedic applications, J. Mater. Sci. Technol. 68 (2021) 76-90.